JGR Space Physics

RESEARCH ARTICLE
10.1029/2023JA031671

Universal Time Effects on Substorm Growth Phases and Onsets

M. Lockwood[1]

[1]Department of Meteorology, University of Reading, Reading, UK

Key Points:

- Universal Time (*UT*) effects in the magnetosphere are caused by the eccentric nature of Earth's intrinsic magnetic field
- There is a *UT* dependence of the open flux (and hence also the integrated magnetopause reconnection voltage) needed to trigger substorm onset
- Growth phases that lead to substorm onset show considerable preconditioning by prior reconnection

Correspondence to:
M. Lockwood,
m.lockwood@reading.ac.uk

Citation:
Lockwood, M. (2023). Universal Time effects on substorm growth phases and onsets. *Journal of Geophysical Research: Space Physics*, *128*, e2023JA031671. https://doi.org/10.1029/2023JA031671

Received 5 MAY 2023
Accepted 23 OCT 2023

Abstract Universal Time (*UT*) variations in many magnetospheric state indicators and indices have recently been reviewed by Lockwood and Milan (2023, https://doi.org/10.3389/fspas.2023.1139295). Key effects are introduced into magnetospheric dynamics by the eccentric nature of Earth's magnetic field, features that cannot be reproduced by a geocentric field model. This paper studies the *UT* variation in the occurrence of substorm onsets and uses a simple Monte-Carlo model to show how it can arise for an eccentric field model from the effect of the diurnal motions of Earth's poles on the part of the geomagnetic tail where substorms are initiated. These motions are in any reference frame that has an *X* axis that points from the center of the Earth to the center of the Sun and are caused by Earth's rotation. The premise behind the model is shown to be valid using a super-posed epoch study of the conditions leading up to onset. These studies also show the surprising degree of preconditioning ahead of the growth phase that is required, on average, for onset to occur. A key factor is the extent to which pole motions caused by Earth's rotation influence the near-Earth tail at the relevant *X* coordinate. Numerical simulations by a global MHD model of the magnetosphere reveal the effect required to generate the observed *UT* variations and with right order of amplitude, albeit too small by a factor of about one third. Reasons why this discrepancy may have arisen for the simulations used are discussed.

Plain Language Summary Earth's magnetic field is eccentric in that the main magnetic (dipole) axis does not pass through the center of the Earth. This introduces a wobble into many aspect of near-Earth space (the "magnetosphere") as Earth rotates. Many consequences of this have been noted in previous papers. This paper investigates the effect of the eccentricity on the phenomenon of magnetospheric substorms. It is shown that the explosive releases of energy stored in the tail of the magnetosphere are more likely to start ("onset") at some Universal Times (and therefore geographic longitudes) than others and an explanation of why is provided.

1. Introduction

1.1. Universal Time Variations in the Magnetosphere

Lockwood and Milan (2023) have recently reviewed Universal Time (*UT*) variations in magnetospheric observations and indices. Their study included: the *am* planetary geomagnetic index (Lockwood et al., 2019; Mayaud, 1972); the *SML* auroral electrojet index (Newell & Gjerloev, 2011a, 2011b); the *SMR* partial ring current indices (Newell & Gjerloev, 2012); the polar cap indices (Lockwood, 2023; Stauning, 2007; Troshichev, 2022), transpolar voltage observations from Low-Earth Orbit (LEO) spacecraft (e.g., Boyle et al., 1997; Hairston & Heelis, 1993), Φ_{PC}; field aligned-current maps derived from measurements by magnetometers on the Iridium LEO satellites by the Active Magnetosphere and Planetary Electrodynamics Response Experiment project (Coxon et al., 2018); and substorm onset occurrence (Forsyth et al., 2015; Newell & Gjerloev, 2011a, 2011b). In addition, Lockwood et al. (2021) have modeled the *UT* variations in the *am* index and its hemispheric sub-indices *an* and *as* and Lockwood et al. (2023) have studied how *UT* variations in the magnetosphere-ionosphere-thermosphere coupled system influence the upper atmosphere Joule heating response to terrestrial Coronal Mass Ejection impacts.

UT effects arise in the coupled magnetosphere-ionosphere-thermosphere system because the Earth's magnetic poles are offset from its rotational axis. The most commonly used model of the intrinsic field of Earth is a geocentric dipole, for which this offset is the same in the two hemispheres. In these models, effects of Earth's rotation in the northern polar regions are equal and opposite to those in the southern polar regions and taking a global average means that many effects cancel and show no net *UT* variation. However, constraining Earth's magnetic dipole axis pass through the center of the Earth is only a useful approximation and eccentric dipole models show that this

is not generally valid. The standard way of describing an eccentric dipole, introduced by Bartels (1936), is to use the first eight coefficients that define a spherical harmonic expansion of the magnetic scalar potential, in models such as the International Geomagnetic Reference Field IGRF (Thébault et al., 2015). This is compared to the first three used to define a centered dipole. In eccentric models the "axial" poles (where the dipole axis threads the Earth surface) are offset from the rotational axis by different amounts in the two hemispheres and these magnetic poles are not separated by 180° in longitude as they are for a geocentric dipole. The eccentric dipole model of Koochak and Fraser-Smith (2017) gives the latitudinal offset of the axial magnetic pole and the rotational pole of 8.23° in the northern hemisphere in 1980 and this fell to 5.91° in 2015. On the other hand, the corresponding values in the southern hemisphere were 15.29° in 1980 and 14.59° in 2015. Hence the ratio of the South/North magnetic pole offsets has risen from 1.86 to 2.47 in just 35 years because the northern magnetic pole has migrated toward the rotational axis. The motion depends on the type of pole considered (there are "dip poles" where the field is vertical as well as geocentric and eccentric dipole poles) but the acceleration of the northern pole has increased in recent years and this is likely to continue; however, although the changes in the core-mantle boundary that have caused this are understood, it is not yet possible to predict future changes (Livermore et al., 2020). Many effects of the offset of the rotational and magnetic poles in the two hemispheres that cancel for a geocentric dipole do not cancel for an eccentric one leaving net *UT* variations. Thus the recent changes in the Earth's intrinsic field mean that *UT* effects in the magnetosphere-ionosphere-thermosphere system are of increasing importance. There are a number of potential effects discussed in the following subsections.

1.2. Ionospheric Conductivity Effects

The most commonly invoked effect of the offsets of the magnetic and rotational poles is that of the changes in ionospheric conductivity at given polar and auroral locations in geomagnetic coordinates. This is because of the changes in solar zenith angles χ at such locations, which modulate the solar-EUV-generated ionospheric conductivities. This effect has been invoked a great many times in the context of *UT* variations in geomagnetic activity (e.g., Lyatsky et al., 2001; Newell et al., 2002; Wang & Lühr, 2007). This mechanism applies to enhanced conductivity that is generated by solar EUV illumination (Ridley et al., 2004) and the effects at a given geomagnetic location are ordered by time-of-year (here quantified by the fraction of a calendar year, *F*) and *UT*. However, conductivity is also enhanced by particle precipitation. This second source is ordered in magnetic coordinates and is highly variable in time (Carter et al., 2020). At certain places and times, the precipitation source is dominant over the EUV source (Kubota et al., 2017). Both EUV and precipitation effects show transient events, the former mainly due to solar flare effects and the latter associated with magnetospheric storms and substorms. In both cases, strong *UT* variations occur as the event evolves but the timing of the events are essentially random in the *UT* of their occurrence and so regular, systematic *UT* variations are not seen. We have had well-established and well-used models of EUV-generated conductivity for several years (e.g., Brekke & Moen, 1993) but the variability, in time and space, of precipitation-induced conductivity has made the development of equivalent models for precipitation effects much more difficult and complex (Carter et al., 2020; Zhang et al., 2015).

The dependence of EUV-generated conductivity at given geomagnetic coordinates on solar zenith angle means there is a dependence on the dipole tilt angle δ with which the Earth's magnetic axis is tipped toward the Sun. In the Solar Geocentric Ecliptic (GSE) frame, the *X* axis points from the center of the Earth toward the center of the Sun, the *Z* axis is the northward normal to the ecliptic and *Y* makes up the right hand set (and so is antiparallel to Earth's orbital motion). In three dimensions, the Earth's magnetic dipole axis $\vec{M}$ makes an angle ψ with the GSE *Z*-axis and we here define the dipole tilt angle δ to be the angle that the projection of $-\vec{M}$ onto the GSE *XZ* plane makes with the *Z* axis. (Note that this definition means that positive δ means that the northern magnetic pole is tilted toward the Sun and the southern away from it and negative δ means the southern/northern pole is tilted toward/away from the Sun). Because Earth's rotational axis is inclined at 23.44° with respect to the *Z* axis, this gives an annual contribution to the variation in δ of ±23.44° which depends on the fraction of the calendar year, *F*. The present paper considers data for 1985–2021, the middle of that interval being 2003. In that year, Earth's geocentric dipole axis made an angle of 10.32° with the rotational axis which gives an additional diurnal variation in δ of this amplitude, making the total range in δ over the year of ±33.76°. For an eccentric dipole, offsets of the north and south magnetic poles in 2003 were 6.81° and 14.96°, respectively, which gives total ranges of δ of ±30.25° and ±38.40° for the north and south poles respectively.

Low values of $|\delta|$ form a characteristic pattern called the "McIntosh" or "equinoctial" pattern with *F* and *UT*. This pattern is also observed in geomagnetic activity, first reported by McIntosh (1959) and frequently discussed

since (e.g., Berthelier, 1976; Cliver et al., 2000; de La Sayette & Berthelier, 1996; Lockwood, McWilliams, et al., 2020; Lockwood, Owens, Barnard, Haines, et al., 2020; Lockwood et al., 2021). The equinoctial pattern is most clearly seen in the *am* index, which responds primarily to the substorm current wedge (Menvielle & Berthelier, 1991). The reason why *am* is the optimum index for observing this pattern is that it has the most uniform *F-UT* response pattern of all geomagnetic indices because it is constructed using homogeneous rings of stations in both hemispheres with weighting function corrections to allow for any unavoidable longitudinal inhomogeneities in the siting of stations due to oceans (Lockwood et al., 2019).

Low δ gives larger solar zenith angles χ at high latitudes which gives lower values in EUV-generated ionospheric conductivity (Moen & Brekke, 1993; Ridley et al., 2004). However, the conductivity pattern depends on δ and not $|\delta|$ and so it is not obvious how conductivities could generate an equinoctial pattern in geomagnetic activity. The proposal of Lyatsky et al. (2001) and Newell et al. (2002) is that global geomagnetic activity is enhanced when the midnight sector of both auroral ovals, where substorms are initiated, are in darkness at E-region heights (solar zenith angles χ greater than about 101°) and so have a lower conductivity, and this only occurs when $|\delta|$ is small. Alternatively, the conductivity variation with χ proposed by Nagatsuma (2004) has, due to slant path effects, a minimum at $\chi = 90°$ (which would be more common at low $|\delta|$). However, this minimum is not present in the models and observations of Brekke and Moen (1993), Moen and Brekke (1993), and Ridley et al. (2004).

It should be noted that, as discussed in the following subsections, EUV-enhanced conductivities in polar regions is far from the only proposed mechanism by which the *F-UT* equinoctial pattern of $|\delta|$ can be imprinted on global geomagnetic activity.

1.3. Dipole Tilt Effects in the Geomagnetic Tail

The near-Earth tail is orientated with respect to the Earth's magnetic axis whereas the mid-tail and far-tail regions are orientated with respect to the solar wind flow (with a small aberration due to Earth's orbital motion). Consequently, between the near-Earth and the mid-tail regions the tail bends through the "hinge angle" which is very close to being the same as the dipole tilt angle δ. Hence this tail hinge angle also shows the equinoctial pattern.

Kivelson and Hughes (1990) proposed that the hinge angle plays a role in the stability of the tail and the triggering of substorm onsets, an idea investigated further by a number of authors (Danilov et al., 2013; Korovinskiy et al., 2018; Kubyshkina et al., 2015, 2022). To fit the observations, substorm occurrence and strength (and hence also global geomagnetic activity) would need to be enhanced when the hinge angle is small (i.e., when $|\delta|$ is small). A variant of this idea was proposed by Alexeev et al. (1996) and Ou et al. (2022) who suggested the dipole tilt effect was through a change in the proximity of the ring current and the closest auroral electrojet.

A different mechanism for generating the equinoctial pattern in the geomagnetic tail has been proposed by Lockwood, McWilliams, et al. (2020) and Lockwood, Owens, Barnard, Watt, et al. (2020). This uses the fact that the dipole tilt influences how quickly open field lines are appended to the tail because of the shift with δ in the magnetic latitude of the magnetic reconnection site in the dayside magnetopause, as has been modeled in numerical MHD simulations (Eggington et al., 2020; Hoilijoki et al., 2014; Lockwood, Owens, Barnard, Watt, et al., 2020; Park et al., 2006) and also observed in satellite data (Kitamura et al., 2016; Trattner et al., 2012; Zhu et al., 2015). In the hemisphere in which the dipole axis is tipped toward the Sun ($\delta > 0$ for the northern hemisphere), open field lines take longer than those in the other hemisphere or for when $\delta = 0$: this is because they have further to travel and because, initially, the open field lines are moving under the magnetic curvature force against, rather than with, the magnetosheath flow. As a result, a larger fraction of the open flux threads the dayside magnetopause sunward of a given X in the tail in the hemisphere tipped toward the Sun (and hence a smaller fraction threads the tail lobe at that X). Numerical simulations show that the total field, in both lobes, is smaller for larger $|\delta|$ and so the magnetic shear across the cross-tail current sheet is greatest for $\delta = 0$ and this too yields an equinoctial *F-UT* pattern (Lockwood, Owens, Barnard, Watt, et al., 2020). This mechanism is supported by the observation that the equinoctial pattern is enhanced by solar wind dynamic pressure which also enhances the magnetic shear across the near-Earth cross-tail current sheet by squeezing the near-Earth tail (Lockwood, McWilliams, et al., 2020; Lockwood, Owens, Barnard, Watt, et al., 2020).

1.4. Ion-Neutral Momentum Exchange

There are other effects of the Earth's dipole tilt. The dynamics of ionospheric plasma is ordered relative to the geomagnetic pole whereas the dynamics of the neutral thermospheric gas is ordered relative to the rotational

pole. Both ion-neutral and electron-neutral collisions contribute to ionospheric conductivities, but ion-neutral collisions have an additional role in momentum exchange between the ionosphere and thermosphere (specifically ions because their greater mass means that they carry much greater momentum than electrons). As a result, plasma convection influences thermospheric winds which, in turn influence the deposition of energy because ion-neutral frictional heating depends on the vector difference between the velocities of ions and neutrals. Hence both the wind response and the effect on energy deposition depend on *UT* (see review in Wang et al. (2017)). An important factor in these effects is temporal variability in the ionospheric convection because the greater number densities of neutrals atoms compared to ions, results in the response times of thermospheric winds to changes in ionospheric flow being larger than the response times of ionospheric flows to changes in magnetospheric dynamics (Lockwood et al., 1988; Zou et al., 2021). Förster and Cnossen (2013) noted that the hemispheric intrinsic magnetic field differences were probably more important for polar thermospheric neutral winds than ionospheric plasma convection but can still influence currents, convection and power dissipation rates in the upper atmosphere and have implications that have been invoked by Cnossen et al. (2012), Förster and Cnossen (2013), and Laundal et al. (2017).

1.5. The Russell-McPherron Effect

The Russell-McPherron (R-M) effect (Russell & McPherron, 1973) is central to understanding the semi-annual variation in geomagnetic activity. A review of the evidence for this mechanism and of its influence has recently been given by Lockwood, Owens, Barnard, Haines, et al. (2020) and Lockwood, McWilliams, et al. (2020). The R-M effect arises because the interplanetary magnetic field (IMF) is ordered, on average, in a solar frame (the Parker Spiral configuration) but coupling into the magnetosphere depends on its orientation relative to Earth's magnetic dipole axis (in a frame such as Geocentric Solar Magnetospheric, GSM). The most appropriate solar frame is the Geocentric Solar Equatorial (GSEQ). The key effect is due to the Earth's dipole tilt: this results in negative IMF $[B_Y]_{GSEQ}$ giving a southward IMF component in GSM (hence enhancing solar wind-magnetosphere coupling) around the March equinox whereas around the September equinox it is positive $[B_Y]_{GSEQ}$ that has this effect. Geomagnetic activity shows, very clearly and very strongly, this preference for high geomagnetic activity at one or other equinox, depending on the polarity of the $[B_Y]_{GSEQ}$ component (Lockwood, McWilliams, et al., 2020; Lockwood, Owens, Barnard, Haines, et al., 2020; Zhao & Zong, 2012). This confirms the key importance of the R-M effect. The diurnal dipole tilt variation due to Earth's rotation means that the September peak (for $[B_Y]_{GSEQ} > 0$) is at around 10 hr *UT* (with a minimum around 22 hr *UT*) whereas the March peak (for $[B_Y]_{GSEQ} < 0$) is at around 22 hr *UT* (with a minimum around 10 hr *UT*).

1.6. Other Dipole Tilt Effects on Magnetopause Reconnection Voltage

The R-M effect has a characteristic *F-UT* pattern which is quite different to the equinoctial pattern in $|\delta|$. Hence the R-M effect does not generate the equinoctial pattern. Another proposal to explain the observed equinoctial pattern in geomagnetic activity is that the magnetopause reconnection voltage Φ_D varies with the dipole tilt (Crooker & Siscoe, 1986; Russell et al., 2003). However (Finch et al., 2008), analyzed the *F-UT* patterns in data from a very large number of individual magnetometer stations and showed that the equinoctial pattern arises in the nightside auroral oval and that it was absent in data from dayside stations. Similarly, Lockwood, McWilliams, et al. (2020) and Lockwood, Owens, Barnard, Haines, et al. (2020) used the mid-latitude $a\sigma$ indices, which cover 6-hr ranges in Magnetic Local Time and showed the equinoctial pattern was strongest in the midnight sector but hardly detectable in the noon sector. This argues against the equinoctial pattern being generated by dipole tilt effects on dayside magnetopause coupling and the magnetopause reconnection voltage Φ_D. These results strongly indicate that the equinoctial pattern in indices such as *am* is not consistent with dipole tilt modulation of the reconnection rate in the dayside magnetopause. However, this does not mean that such effects do not occur and numerical simulations by global MHD models have found dipole tilt modulation of the reconnection voltage and in cross-tail current sheet. This is discussed further in Section 6.

1.7. Inductive Effect of Pole Motions

Recently another mechanism has been added to this list. This is, in effect, a different manifestation of the effect of dipole tilt on the evolution of open flux tubes into the tail proposed by Lockwood, Owens, Barnard, Watt,

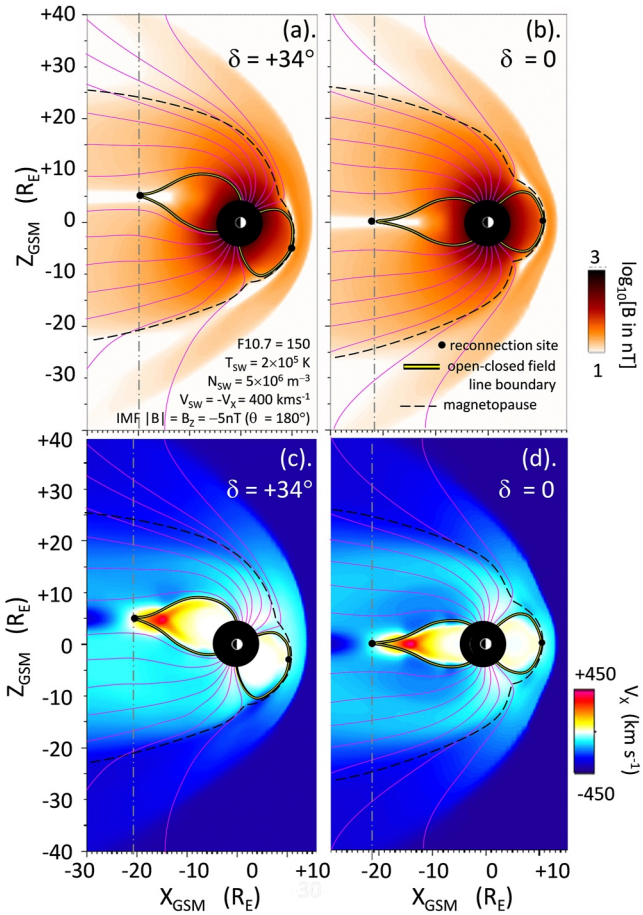

Figure 1. Numerical MHD model results from the SWMF model (version v20140611—also known as BATSRUS) for run time 90 min in the simulations described by Lockwood, Owens, Barnard, Watt, et al. (2020). Note these simulations use a geocentric dipole model of the Earth's intrinsic field. The plots show noon-midnight cuts in the Solar Geocentric Ecliptic *XZ* plane ($Y = 0$), panels (a, b) give color contours of the magnetic field strength, B (on a logarithmic scale) and panels (c, d) give color contours of the sunward flow speed, V_X. Panels (a, c) are for a dipole tilt of $\delta = +34°$ and panels (b, d) are for $\delta = 0$. The magnetopause, defined from the plasma beta, flow, and the magnetopause current in the Y direction, is shown as dashed lines and reconnection sites, identified by polarity flips in fast flows in the relevant direction, by black dots. The black and yellow line is the open-closed field line boundary. In addition, open magnetic field lines, reconnected 4 min apart, are shown in mauve. The vertical gray dot-dash line is at the X value of the tail reconnection X-line (at $Y = 0$) which is at $X = -20.5\ R_E$ for $\delta = +34°$ and $X = -21\ R_E$ for $\delta = 0$.

et al. (2020) that was discussed in Section 1.3. Lockwood et al. (2021) have noted that models and observations show that the ionospheric polar caps and auroral ovals undergo almost the same diurnal sunward and antisunward sequence of motion due to Earth's rotation as the geomagnetic pole in a geocentric-solar frame (meaning any frame that has an X axis that points from the center of the Earth to the center of the Sun, such as GSE, GSM, and GSEQ). At first sight the velocities of these motions appear negligible, being smaller than typical solar wind flow speeds in the same frame by a factor of order 2×10^{-4}. However, the flow-transverse magnetic field is larger in the ionosphere than in interplanetary space by a factor that is typically 10^4 and hence in terms of electric fields and voltages the pole motions give values that are typically about half those in interplanetary space.

As demonstrated by Kabin et al. (2004), the effect of dipole tilt on the location of the open-closed field line boundary is readily seen in simulations made by numerical, global, MHD models of the magnetosphere. Figure 1 shows simulations by the SWMF numerical MHD model (version v20140611, also known as BATSRUS) with a geocentric dipole model of the intrinsic geomagnetic field. The solar wind at (and before) the run time used here (90 min) was steady at 400 km s^{-1} with an IMF pointing due southward in the GSM frame and of magnitude 5 nT. The solar wind number density was 3×10^6 m^{-3} and the mean ion mass 1.1 amu. Using the empirical relation by Lockwood and McWilliams (2021a), the predicted magnetopause reconnection voltage Φ_D is constant at 56 kV. Note that in order to isolate the effects of the dipole tilt angle δ, these simulations were carried out with two fixed values of δ (0 and 34°) and not one that varies with *UT*. Note also that the model has been run over 90 min to give a near steady-state with the effect of initial conditions removed.

Figure 1 shows noon-midnight cuts (i.e., in the *XZ* plane of the GSE frame) of the modeled structure in field strength (top panels) and antisunward flow speed (bottom panels) with the left-hand panels for a dipole tilt of $\delta = +34°$ and the right-hand panels for $\delta = 0$. Plots for $\delta = -34°$ are not shown because, for the geocentric dipole used, the results for the northern hemisphere are the same as for the southern for $\delta = +34°$. The magnetopause is shown by the black dashed line and the X value of the tail reconnection site by the vertical gray dot-dash line. The mauve lines are open field lines that were reconnected 4 min apart. The symmetry of the $\delta = 0$ case means that the open field line motion into the tail is the same in the two hemispheres and Figure 1d shows that in both hemispheres open field lines have the same antisunward speed at the magnetopause at all X and that in both hemispheres open field lines take about 12.5 min for the point where they thread the magnetopause to move from the magnetopause reconnection site to the X coordinate of the tail reconnection site ($X \approx -21\ R_E$): as a result, in Figures 1b and 1d in both hemispheres the two most recently reconnected field lines shown thread the magnetopause sunward of this X value, and the other five of the open field lines shown are appended to the tail lobe by this X: hence roughly (5/7) ≈ 70% of the open flux is appended to both tail lobes at this X in this case.

Figures 1a and 1c show how radically the dipole tilt alters this hemispheric symmetry. The field lines in the northern hemisphere reach a flow speed of $V_X = 200$ km s^{-1} at a GSE latitudes near 80° latitude (approximately 12 min after reconnection) whereas those in the southern hemisphere reach it at near 45° (after only 2.5 min). This is because the shift of the magnetopause reconnection site into the southern hemisphere means that for southern hemisphere open field lines the sheath flow and the tension force act together to move open flux tailward whereas initially the sheath flow is opposing the motion of northern hemisphere open flux toward the tail. As a result of this hemispheric difference in open flux evolution, only 4 out of the 7 open field lines are inside the tail lobe

at the X of the tail reconnection site (approximately 60%) in the northern hemisphere, whereas in the southern hemisphere this figure is 6 out of 7 (approximately 86%).

The tilt of $\delta = 34°$ used in Figure 1 is an extreme deviation from $\delta = 0$, slightly larger than the peak-to-peak diurnal variation of the southern ionospheric polar cap over 12 hr of 29.92° (for the pole offset in an eccentric dipole in 2003) and a bit over twice the corresponding diurnal range for the northern polar cap of 13.62°. However it clearly demonstrates how the polar caps move sunward and antisunward with the value of δ. The model runs shown in Figure 1 will be used in Section 5 to check that a best-fit value of a parameter used in this paper (R_X, defined in Section 2.1) is reasonable.

There is also diurnal motion of the ionospheric polar caps in the Y-direction, but this is different in the GSE, GSM, and GSEQ frames as they differ in their Y-axis definition; however, they share the same X axis and so the polar cap motion in this direction (toward/away from the Sun) is the same in all these frames and here termed V_P (V_{PN} in the northern hemisphere, V_{PS} in the southern). Assuming there is no change in the polar cap shape, the dawn-dusk voltage across the polar cap generated by these pole motions in all three frames is

$$\phi = V_P B_i d_{PC} \tag{1}$$

where B_i is the ionospheric magnetic field and d_{PC} is the maximum diameter of the polar cap in the dawn-dusk direction, perpendicular to X. Note that d_{PC}, V_P, and B_i are all values for the same altitude. We define V_P as positive for motion toward the Sun which is in the opposite direction to the solar wind flow (which is close to the -X direction). For this definition, the voltage ϕ given by Equation 1 is subtracted from that generated across the polar cap by the solar wind flow because it is positive when the polar cap is moving sunward. Using the Expanding-Contracting polar cap model of ionospheric convection excitation (Cowley & Lockwood, 1992; Lockwood & Cowley, 2022; Lockwood & McWilliams, 2021b; Milan et al., 2021), the total voltage across the polar cap allowing for this pole motion effect becomes

$$\Phi_{PC} = f_D \Phi_D + f_N \Phi_N + \Phi_V - \phi \tag{2}$$

where Φ_D is the reconnection voltage in the subsolar dayside magnetopause (the rate of production of open flux), Φ_N is the reconnection voltage in the cross-tail current sheet that is between open flux in the tail lobes (the rate of loss of open flux), Φ_V is the "viscous-like" voltage induced by all non-reconnection mechanisms of solar wind-magnetosphere interaction. The factors f_D and f_N are the fractions of reconnection voltages (Φ_D and Φ_N, respectively) placed across the maximum diameter of the polar cap. These factors depend upon the shape of the polar cap and how it is changing: for the approximation of a polar cap that remains circular at all times $f_D = f_N = 0.5$ (Lockwood, 1993) but in general the polar cap boundary shape is always evolving (Tulegenov et al., 2023) and so the factors f_D and f_N are not constant.

It is worth noting that the Y-direction motion of the polar cap is likely to also have some effects, for example, causing deformations of the ionospheric convection pattern, as illustrated schematically by Lockwood (1991). These diurnal motion effects of the polar cap would also be superimposed on the effect caused by the IMF Y-component described by Cowley et al. (1991) and are likely to add to the twist of the tail caused by IMF B_Y (Pitkänen et al., 2016) and hence the location of substorm onset (Østgaard et al., 2004), although some studies suggest such effects require a strong IMF B_Y that persists longer than the diurnal cycle of the pole motions (Milan et al., 2010). There are also indications that this can influence the occurrence of substorm onset (Liou et al., 2020).

Figure 2 looks at the implications of the pole motions by considering a Faraday loop PASGUC that is fixed in the GSM frame (shown by the yellow dashed line). The segment PC is the polar cap diameter and the voltage along it (i.e., the magnetic flux transfer rate across it) is $\Phi_{PC} = V_i B_i d_{PC}$ where V_i is the plasma and frozen-in field velocity. The segment SG is just outside the bow shock in interplanetary space (sometimes referred to as the "Stern Gap") and the voltage across it is $\Phi_{SG} = V_{SW} B_Z d_{SG}$, where V_{SW} is the solar wind speed in the -X direction, B_Z is the IMF component in the GSM Z direction and d_{SG} is the spatial separation of S and G in the GSM Y direction (the width of the Stern gap). The segments of the loop PAS and GUC are the open field lines on the dawn and dusk extremities of the polar cap and neglecting any field-aligned voltages (that will be very small compared to Φ_{SG} and Φ_{PC}), Faraday's law tells us the difference in the flux transfer rates $\Phi_{SG} - \Phi_{PC}$ is equal to the rate of growth of flux threading the loop PASGUC. Because the solar wind and relevant sheath flow are supersonic

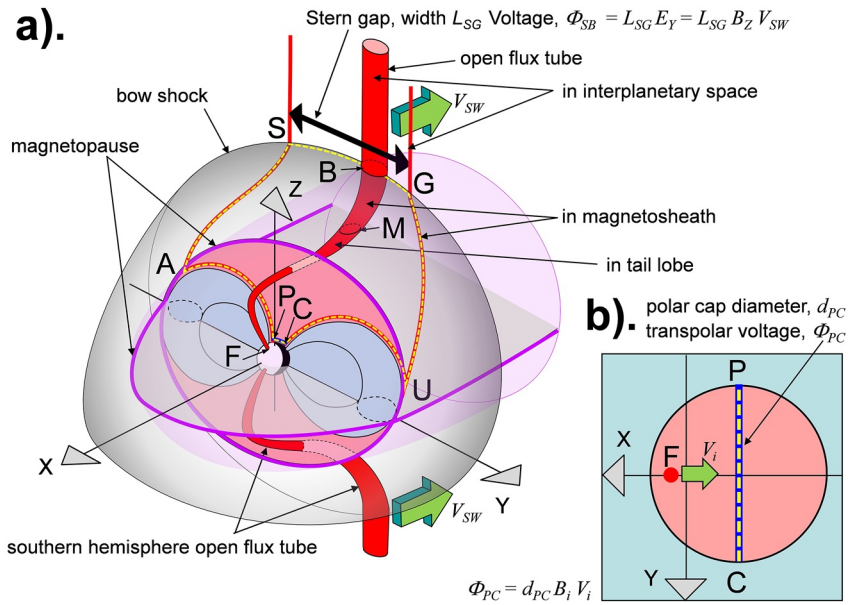

Figure 2. (a). Schematic of inductive decoupling of the "Stern Gap" voltage across open field lines in interplanetary space, Φ_{SG} and the transpolar voltage in the ionosphere Φ_{PC}. The magnetosphere is here viewed from northern middle latitudes in the mid-afternoon sector. The loops PASGUC (shown by the yellow dashed line) and PAUC (enclosing the northern tail lobe cross-section shaded pink) are fixed in the *XYZ* GSM frame, where P and C are the dawn and dusk extremes of the northern ionospheric polar cap, AP and UC are field-aligned in the magnetosphere, SA and GU are field-aligned in the magnetosheath, SG lies immediately outside the bow shock and AU in the tail magnetopause. The red flux tubes are open field lines and the northern-hemisphere tube threads the bow shock at B and the magnetopause at M and has an ionospheric footpoint, F. The solar wind flow is in the $-X$ direction at speed V_{SW}. (b) Is a view looking down (in the $-Z$ direction) on the northern hemisphere polar cap in which the antisunward ionospheric convection velocity of the footpoint F is V_i. After Lockwood and Milan (2023).

and super-Alfvénic, the solar wind flow and voltage Φ_{SG} is not influenced by any change in Φ_{PC} caused by the pole motion. Hence, in addition to reducing the transpolar voltage Φ_{PC} by ϕ, the effect of a sunward pole motion ($\phi > 0$) is to increase the lobe flux by ϕ.

Hence the diurnal cycle of sunward and then antisunward pole motion caused by the rotation of the Earth generates a diurnal cycle of decrease then increase of the ionospheric transpolar voltage with an associated cycle of increase and then decrease in the rate at which open flux is added to the tail lobe.

1.8. Universal Time Variations

Many of the effects discussed above generate systematic *UT* variations when a subset of the data are considered but not when averages of all data are considered. For example, the R-M effect generates *UT* variations if we consider the two polarities of the IMF separately, but because the distribution of IMF B_Y values is very close to symmetric around zero, the effects of the two polarities almost completely cancel in a full data set and so the R-M effect does not give a net systematic *UT* variation if all data are considered.

Indeed, because the dipole tilt angle averages to zero over a full year, this is true for any mechanism that depends linearly on the dipole tilt. However, EUV-induced ionospheric conductivities have a non-linear dependence on solar zenith angle and hence on the dipole tilt. This means that the conductivity effects can give a net systematic *UT* variation even after averaging over a whole number of years. However, this depends on location, as demonstrated by Figure 6 of Lockwood and Milan (2023).

The pole-motion effect is different because the diurnal variation of the sunward velocities V_{PN} and V_{PS} are almost independent of the time of year (Lockwood et al., 2021) and so their diurnal effect is not reduced or eliminated by averaging over a whole number of years.

Because the offset of the rotational and magnetic pole in the southern hemisphere is approximately twice that in the northern, the amplitude of the sinusoidal variation in the pole motion speed V_{PS} is approximately twice that

in V_{PN} and so the effects on ionospheric transpolar voltage and lobe flux growth rate are roughly twice as large in the south than the north. In addition, whereas the sinusoidal variations would be in exact antiphase (and of equal amplitude) for a geocentric dipole model of the field (and hence would be equal and opposite and so cancel at any one time), the longitudinal separation of the axial poles for an eccentric dipole is not 180° and the hemispheric variations are not in exact antiphase as well as being different in amplitude. Thus there is a net *UT* variation for a global average for an eccentric dipole that is absent for a geocentric dipole. The longitudinal separation of the poles from the Koochak and Fraser-Smith (2017) eccentric dipole model has fallen from 152° in 1985 to 145° in 2015. This means that the phase difference between the sinusoidal variations in V_{PS} and V_{PN} has decreased from 0.85π to 0.81π, compared to the constant value of π for a geocentric dipole.

2. The Effect of Pole Motions on Substorm Growth Phases

2.1. A Simple Monte-Carlo Model of Substorm Growth Phases and Onsets

Lockwood and Milan (2023) have recently proposed a simple Monte-Carlo model of how pole motions influence substorm growth phases and so introduce a *UT* variation into substorm onset occurrence. This section refines that model slightly and Section 3 provides an independent test of the concepts it is based on. In this model, the magnetopause reconnection voltage Φ_D is assumed constant and, because we are aiming to reproduce average behavior, we use the overall average $\langle\Phi_D\rangle$ of 24 kV. In Lockwood and Milan (2023), the nightside reconnection voltage Φ_N was also held constant. In the present paper the linear open flux loss found by Lockwood et al. (2023) for times of small $|SML|$ is used, with the loss time constant of $\tau_N = 6.8$ hr $= 2.448 \times 10^4$ s reported in that paper. Thus the open flux continuity equation for the growth phases simulated is

$$dF_{PC}/dt = \Phi_D - \Phi_N = \Phi_D - F_{PC}/\tau_N \quad (3)$$

The questions then arise "when do growth phases end?" and "what triggers substorm onset?." This has been discussed for many years and many mechanisms proposed (Lyons et al., 2018; Milan et al., 2019; Spence, 1996; Tanaka et al., 2021). To determine when onset occurs, the model uses the concept from the analysis of F_{PC} values at the time of onset by Boakes et al. (2009): this does not define the precise time of onset but does give us a useable statistical relationship. These authors found that for values of F_{PC} below 0.3 GWb, the probability of a substorm onset occurring was negligible but that as F_{PC} rose above this level the probability increased linearly and was undefined above 0.9 GWb. Lockwood and Milan (2023) took the probability of onset to become unity at $F_{PC} = 1.2$ GWb, the maximum possible open flux estimated by Mishin and Karavaev (2017). The implication of the dependence of the probability of onset being set by the magnitude of the open flux F_{PC} that it is set by the size of the cross-tail current (i.e., the magnetic shear between the two tail lobes) which increases with F_{PC}, at least at distances from the Earth small enough for solar wind dynamic pressure to cause the lobe fields to rise with increased F_{PC}. (Further down the tail, where the magnetopause becomes aligned with the solar wind flow, increased F_{PC} causes the tail to flare but the field in the lobe is set by the static pressure in the solar wind (Lockwood, 2013)). The flux in one tail lobe, $[F_{lobe}]_X$, at a given (negative) value of X in the tail, is given by

$$[F_{lobe}]_X = F_{PC} - F_X \quad (4)$$

where F_X is the open flux connected to the ionospheric polar cap in that hemisphere that still threads the dayside magnetopause sunward of X. Differentiating with time t gives

$$d[F_{lobe}]_X/dt = dF_{PC}/dt - dF_X/dt \quad (5)$$

The pole motion influence on F_X depends on the value of X considered and will decline with distance away from the Earth down the tail. We can allow for this with a factor that depends on X, R_X, which is the ratio $(dF_X/dt)/\phi$,

$$d[F_{lobe}]_X/dt = dF_{PC}/dt - R_X\phi \quad (6)$$

The factor R_X will, in general, depend on how much of the open flux was recently opened and hence the prior history of the voltage Φ_D. However, the constant Φ_D used in this simple model means that R_X will be constant for a given X. Substituting from Equation 3 gives

$$d[F_{lobe}]_X/dt = \Phi_D - F_{PC}/\tau_N - R_X\phi \quad (7)$$

Note that Equation 7 applies to both hemispheres and that, because of Maxwell's equation $\nabla.\vec{B} = 0$, Φ_D and F_{PC} are the same for both hemispheres, as is the loss time constant τ_N. On the other hand, from the discussion in Section 1.7, we need to separately consider $(R_{XN}\phi_N)$ for the northern hemisphere and $(R_{XS}\phi_S)$ for the southern in order to compute the total tail lobe flux $[F_{tail}]_X$, which is the sum of the north and south lobe fluxes at X, $[F_{lobe}]_{XN}$ and $[F_{lobe}]_{XS}$:

$$d[F_{tail}]_X/dt = d[F_{lobe}]_{XN}/dt + d[F_{lobe}]_{XS}/dt = 2\Phi_D - 2F_{PC}/\tau_N - R_{XN}\phi_N - R_{XS}\phi_S \quad (8)$$

The survey by Boakes et al. (2009) found that substorm onset probability increased with the open flux F_{PC}. The model of substorm growth phases employed here uses the equivalent of the Boakes et al. (2009) result but also allows for the open magnetic flux that threads the dayside magnetopause, F_X and how it is influenced by the dipole tilt. It is proposed that the probability of onset being triggered primarily depends on the level of $[F_{tail}]_X$, rather than F_{PC}. In order to demonstrate the principle, the ratios R_{XS} and R_{XN} are taken to be equal and held constant. The value was varied and the optimum fit to the observed *UT* variation of substorm onset (see Section 2.3) was found for $R_{XS} = R_{XN} = 0.15$ for the X coordinate relevant to substorm onset. In Section 3 this value is also shown to be consistent with a superposed epoch analysis of substorms onsets.

Because sequences of upstream IMF variation are independent of the phase of Earth's rotation, the model initiates each growth phase at a *UT* that is selected using a random number generator. The integration of Equation 8 is started from an initial tail lobe flux (in each lobe) of $F_i = 0.2$ GWb ($[F_{tail}]_X = 0.4$ GWb) which is consistent with typical quiet time values of F_{PC}. Note that, in reality, this value will vary but that lowering F_i increases the average length of the growth phases but does not influence the distribution of onset *UT*s because the start *UT* values of growth phases are randomly selected. Using Equation 3, the value of F_{PC} throughout the growth phase is also computed and by assuming a circular polar cap this yields the polar cap diameter, d_{PC} (using the equation by Lockwood et al. (2023), based on the work of Milan et al. (2021)). This is used in Equation 1 to compute ϕ_N and ϕ_S at each time. The model calculates $[F_{tail}]_X$ every 1 s using Equation 8 and onset is determined to have occurred or not at each time step using a random number generator constrained to select onset occurrence based on the probability set by the $[F_{tail}]_X$ value. Note that there are three improvements in the model used here, compared to that used by Lockwood and Milan (2023): (a) it allows for the effect of growth in F_{PC} on the open flux loss rate Φ_N and (b) it allows for the effect of changing polar cap diameter d_{PC} on the pole-motion voltage ϕ (Equation 1) and (c) it allows for the R_X factors.

This model is purely a model of substorm growth phases and onset and so cannot reproduce the intervals between onsets, Δt_o, because they also include the durations of the subsequent expansion and recovery phases (or alternatively the period of driven reconnection as discussed by Milan et al. (2021)) and any interval of quiet (northward IMF) conditions between the substorms. Also notice that each substorm growth phase in the model starts from the same initial tail flux $2F_i$ and at a randomly selected *UT*. Hence the model cannot account for recurrent substorms during periods of persistent southward IMF, where a growth phase of a substorm starts immediately after the recovery phase of the prior substorm.

2.2. Effects of Pole Motions on Transpolar Voltages and the Accumulation of Magnetic Flux in the Tail Lobes

Figures 3b and 3d show idealized variations that give an indication of how the pole motions influence the transpolar voltage and the accumulation of lobe flux at the X relevant to onset. This plot is illustrative and for constant values of the reconnection voltages Φ_D and Φ_N. The value of Φ_N and of the polar cap diameter d_{PC} employed would apply for a polar cap flux of $F_{PC} = 0.54$ GWb. The key point is that effects of the pole-motions in the two hemispheres are not of equal amplitude nor in perfect antiphase, as they would be for a geocentric dipole. As a result, there is a sinusoidal variation in both the average Φ_{PC} and the average $\Delta[F_{lobe}]_X$ which is the integral of $R_X\phi$ with time. Figure 3c is for steady-state ($\Phi_D = \Phi_N$) whereas Figure 3d is for a growing polar cap with $\Phi_D = 24$ kV and $\Phi_N = 22$ kV. Figure 3d shows that, compared to the case without pole motions (the dashed black line), the net effect of the *UT* variations is to reduce the rate at which flux is added to the tail between 2.5 hr *UT* and 14.5 hr *UT* but to enhance it at all other *UT*s.

2.3. The *UT* Distribution of Substorm Onsets

Figure 4a shows the histograms of the numbers of substorm onsets N_o in *UT* bins 0.5 hr wide, derived for 1985–2020 (inclusive) from the *SML* index and using the algorithm by Forsyth et al. (2015) (hereafter FEA).

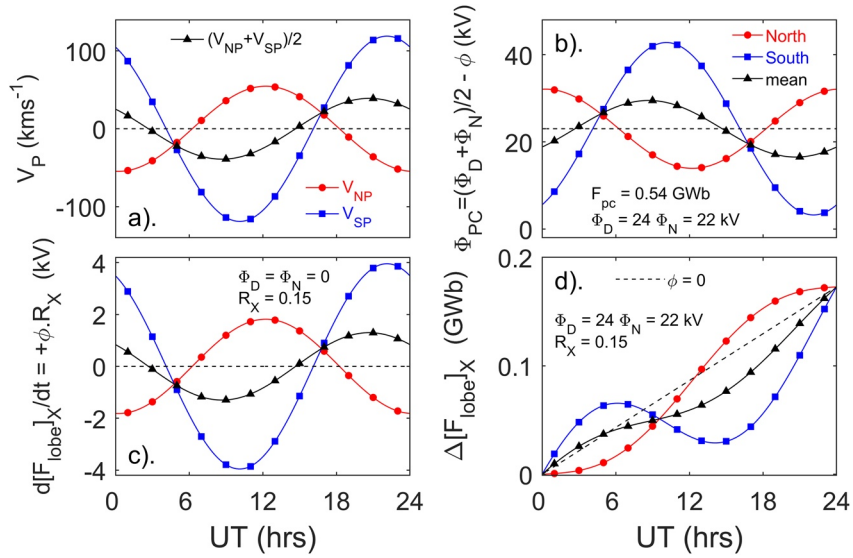

Figure 3. Plots of idealized Universal Time (*UT*) variations caused by pole motions. In all plots the red lines with red circle symbols are for the northern hemisphere polar cap, blue lines with blue square symbols are for the southern hemisphere polar cap and black lines with triangle symbols are for the global average of the two. Note that the symbols are added to aid readers with impaired color vision and spaced considerably further apart than the *UT* resolution of the plots which is 1 min. Variations are based on the eccentric dipole model of Koochak and Fraser-Smith (2017) for the year 2003. (a) The speed of sunward motion in the GSM frame of the geomagnetic poles at 120 km altitude in the E-region ionosphere, V_{NP} in the north, V_{SP} in the south and the average of the two in black. (b) The polar cap voltages Φ_{PC} from Equations 1 and 2 for constant dayside reconnection voltages of $\Phi_D = 24$ kV and a constant nightside voltage of $\Phi_N = 22$ kV (the value we would expect at low—*SML* activity levels for an open flux of $F_{PC} = 0.54$ GWb for the linear loss dependence with time constant $\tau_N = 6.8$ hr). The viscous-like voltage Φ_V is set to zero. For a circular polar cap this F_{PC} gives a polar cap diameter of $d_{PC} = 3.71 \times 10^6$ m. (c) The contribution of the pole motions to the rate of accumulation tail lobe flux at *X* (for $R_X = 0.15$), $d[F_{lobe}]_X/dt = R_X.\phi$ that would be the only change if steady state applied with $\Phi_D = \Phi_N$. (d) The total accumulation of lobe flux $\Delta[F_{lobe}]_X$ for the values of Φ_D, Φ_N in panel (b). The dashed black line is for $\phi = 0$.

The onset list by Newell and Gjerloev (2011a) and Newell and Gjerloev (2011b) (hereafter N&G) gives a very similar variation. The total number of substorm onsets ΣN_o is 88,439 for the FEA list and 62,532 for the N&G list. Hence the FEA list includes more and smaller events that are not counted as distinct onsets in the N&G list. Despite this difference, the distribution in *UT* is similar in the two cases with a large peak near 12 hr *UT*. This is broadly reproduced by the simple Monte-Carlo model, as shown by the mauve lines in Figure 4a. In the model, this occurs because the slower than average rate of accumulation of tail lobe flux that starts at around 3 hr *UT* means that fewer simulated growth phases (that remember were started at randomly chosen *UT*s) are reaching the required tail lobe flux to give a lower probability of onset at those *UT*s. After 10 hr *UT* the rate at which growth phases reach the onset threshold rises again because the rate of increase in tail flux has grown due to the poole motions. The observed mean time between onsets Δt_o is shown by the blue histogram in Figure 4b: as discussed in Section 2.1, this cannot be reproduced by the model. However, the observed Δt_o also shows a marked variation with *UT*: it decreases from near 4 hr to close to 3 hr over the interval 5–12 *UT* while the number of onsets N_o rises. However after 12 *UT* it remains low even though N_o falls again. This shows that although substorm onsets are rarer by 15 *UT*, the events that do occur tend to recur in short succession. As discussed in Section 2.1, this behavior cannot be captured in the model which restarts each growth phase at a random *UT* and so it is not surprising the observed variation cannot be reproduced by the model at these *UT*s in Figure 4a. However, the model does explain how the dipole tilt effect gives the observed peak in onset occurrence at around 12 *UT*.

It is interesting to note what is happening in the growth-phase model. Initially the open flux F_{PC} is low and so the nightside reconnection voltage Φ_N is considerably smaller than the dayside voltage Φ_D. This means the polar cap flux grows rapidly. However, the rise in F_{PC} increases the value of Φ_N and the rise in F_{PC} slows. Eventually the difference between Φ_D and Φ_N becomes small and so the lobe flux variations due to the diurnal pole motions and, in particular, the variations that they cause in $[F_{lobe}]_X$ become significant. Hence although variations in $[F_{lobe}]_X$ due to the pole motions are small they have a significant impact on when the total tail field $([F_{lobe}]_{XN} + [F_{lobe}]_{XS}$ reaches a value that makes the probability of an onset occurring high.

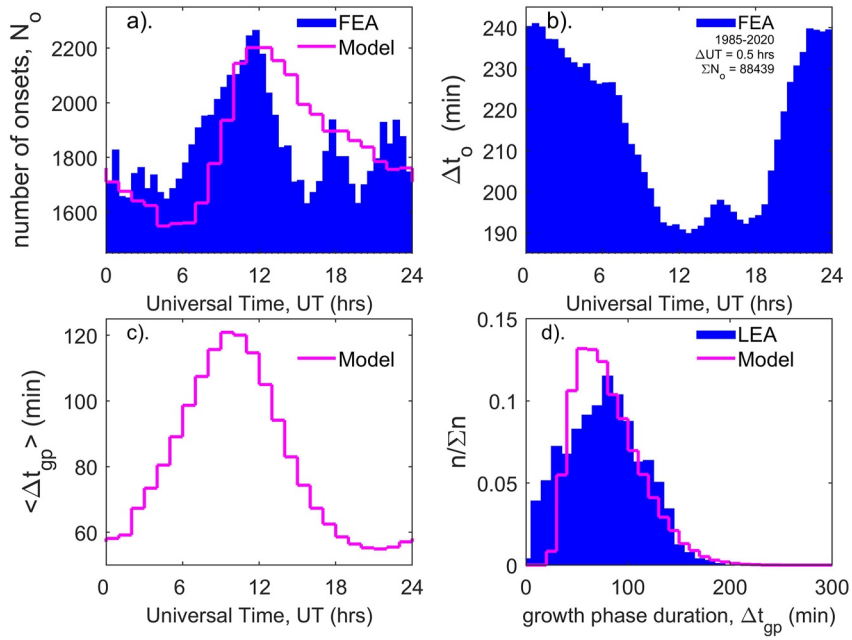

Figure 4. The blue histograms in the top panels show observed distributions with *Universal Time* (*UT*) of (a) substorm onset times and (b) the interval after the prior onset from the list of such events compiled for 1985–2020 (inclusive) using the *SML* index and the algorithm by Forsyth et al. (2015). These plots both show a marked *UT* variation. The mauve line in panel (a) is the variation predicted by the simple Monte-Carlo model described in Section 2.1. (c) Means of the modeled growth phase duration in bins $\Delta UT = 1$ hr wide, $\langle \Delta t_{gp} \rangle$, as a function of the *UT* of onset. (d) The probability distribution of modeled growth phase durations Δt_{gp} (mauve line), where n is the number in bins 10 min-wide bins and Σn is the total number (equal to 200,000 for the model simulations). Also shown by the blue histogram is the distribution for $\Sigma n = 368$ observed growth phase durations compiled by Li et al. (2013).

Figure 4c presents the *UT* variation in the mean of the modeled growth phase durations Δt_{gp}. Unfortunately, we do not have a large observational database to compare these predictions to. However, the plot confirms the above interpretation of the model predictions, with the growth phases coming to an end at around 12 *UT* having greater durations on average. Figure 4d shows the overall distribution of the 200,000 simulated Δt_{gp} values (in mauve) is quite similar to that of the 368 values observed by Li et al. (2013) (hereafter LEA), shown by the blue histogram. LEA divided the onsets into a high, medium and low subsets of the interplanetary electric field, E_{SW}, and showed that the distribution of Δt_{gp} values shifted to lower values for the larger E_{SW} cases, as we would expect. The distribution shown by the blue histogram in Figure 4d is the total for all three E_{SW} subsets. The mean value of the LEA distribution is 77 min which is close to the value of 81 min for the modeled distribution. The major difference is that the modeled distribution has fewer very short growth phases which suggests that either the initial total lobe flux F_i is slightly too low or that the threshold tail flux of 0.6 GWb for the probability of onset rising above zero is slightly too high.

3. Superposed Epoch Analysis of Substorms

Section 2.3 shows that the simple Monte-Carlo model described in Section 2.1, whilst not fully modeling the observed *UT* variation of substorm onsets, provides an important insight into dipole tilt effects. In this section we look for more direct evidence of such an effect using analysis of the variations in the *SMU* and *SML* geomagnetic indices and in the magnetopause reconnection voltage estimated from interplanetary measurements, Φ_D, using a superposed-epoch analysis (also known as Chree analysis or compositing). This paper presents the plots made using the FEA onset list, but results for the N&G list were similar.

Figure 5 presents superposed-epoch plots of the variations in (a) *SML*, (b) *SMU*, and (c) Φ_D. The epoch time is relative to the times t_o of each of the 88,439 substorm onsets in the FEA list for the years 1985–2020, inclusive. The mean value and the standard error in the mean are computed at epoch times $(t - t_o)$ between −240 and +240 min in steps of $\delta t = 1$ min. This was repeated using randomly selected epoch times t_o as a test of

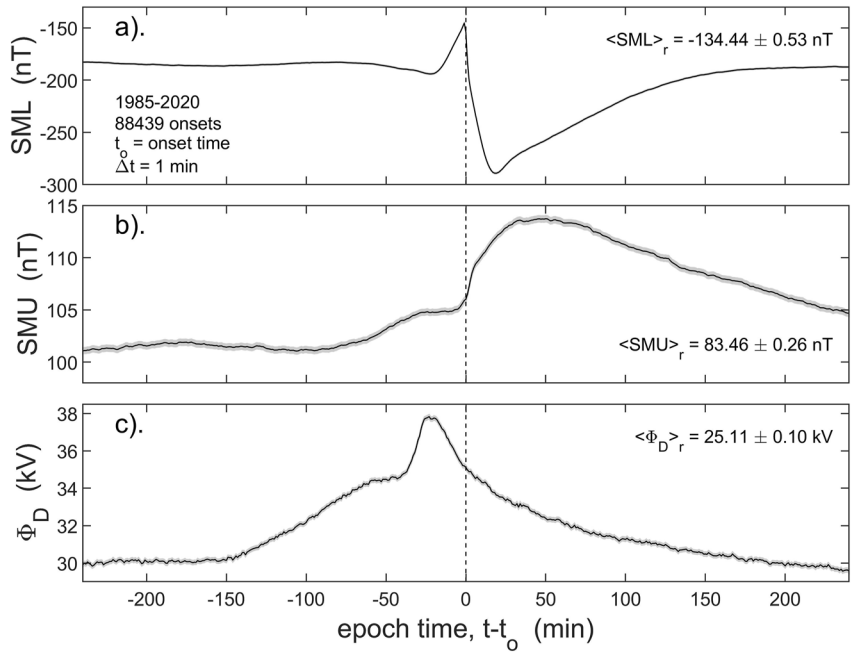

Figure 5. Superposed-epoch plots of substorms using the FEA list of substorm onsets for 1985–2020, inclusive. The mean value is shown as a function of epoch time ($t - t_o$), where t is the observation time and t_o is the time of onset, for: (a) the *SML* index; (b) the *SMU* index; and (c) the estimated reconnection voltage, Φ_D, lagged by a nominal propagation lag of $\delta t_p = 19$ min from the nose of the bow shock using the formula derived by Lockwood and McWilliams (2021a). The gray areas under the plotted black line are between plus and minus one standard error in the mean, but because of the very large number of samples (88,439) these areas are often smaller than the line width used and cannot be seen (particularly for *SML*).

significance: because of the very large numbers of samples, these random tests gave a completely flat variation: these are not shown in Figure 5 as values are considerably lower and so showing them suppresses detail in the plots for the real t_o; however each plot gives the mean for the randomly selected epoch times (respectively, $\langle SML \rangle_r$, $\langle SMU \rangle_r$ and $\langle \Phi_D \rangle_r$ in Figures 5a–5c), plus and minus the value of the mean of the corresponding standard errors. The randomly selected onset values are shown in Figure 8 which presents the superposed-epoch plots at lower time resolution but over considerably larger ranges of epoch time, ($t - t_o$).

In Figure 5, the black lines are the mean values over-plotted on top of gray bands that are plus and minus the standard error in the mean. Because of the very large numbers of samples, the gray band is hardly visible, especially for *SML*. The vertical black dashed line is at epoch time ($t - t_o$) = 0. The Φ_D data have been lagged by a nominal propagation lag of $\delta t_p = 19$ min from the nose of the bow shock. This value is appropriate to the transpolar voltage Φ_{PC} and *SML* response to Φ_D (Lockwood & McWilliams, 2021b), but values near 30–40 min would be more appropriate to the delay before substorm onset and *SML*. Hence in relation to onset the Φ_D curve in Figure 5c may need to be shifted to the left by an additional lag of about 10–20 min in some considerations.

The variation in *SML* in Figure 5a is as expected with some small changes in the growth phase shortly before onset and a big perturbation to large negative values starting at onset. It should be remembered the onset times are determined from *SML* and so we would expect *SML* to be well ordered by the onset times t_o derived from it. The variation in *SMU* is also as expected with small increases in the growth phase and then larger positive values after onset. Note that for the randomly selected values of t_o the values (almost identical at all epoch times) are $\langle SML \rangle_r = -134.44 \pm 0.53$ nT and so larger (less negative) than for the real epoch times and values of $\langle SMU \rangle_r = 83.46 \pm 0.26$ are considerably lower. Hence in all of the 8 hr of epoch time shown, the disturbance levels of *SML* and *SMU* are considerably above the overall average values. Similarly $\langle \Phi_D \rangle_r$ is 25.11 ± 0.10 kV at all epoch times and so considerably lower than for the 8 hr-period around substorm onset.

Figure 6 is the same as Figure 5c, but also shows the results for two 1-hour windows of the *UT* of the onset. The windows shown are 15–16 *UT* (in red) and 02–03 *UT* (in blue). These *UT* ranges are chosen as they give the maximum deviation either side of the values for all onsets. The means are taken over Δt of 5 min (rather than

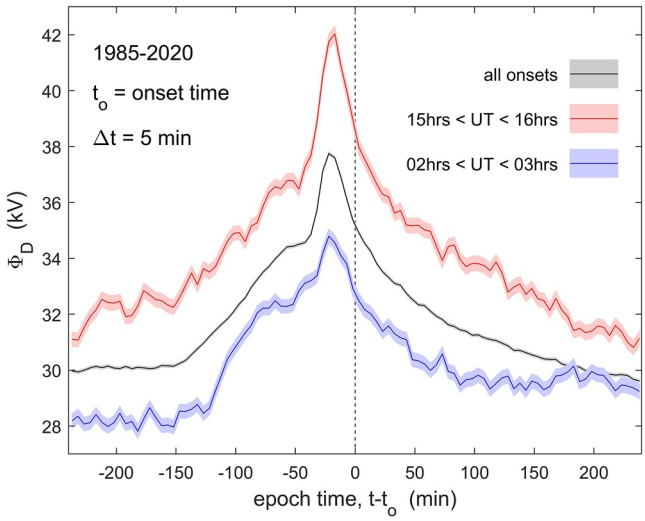

Figure 6. The same as Figure 5 but showing the values for onset *Universal Time* (*UT*) between 15 and 16 hr (in red) and between 02 and 03 hr (in blue). The pink and pale blue shaded areas are plus and minus one standard error in the mean. The averages are here taken over $\Delta t = 5$ min windows in epoch time, $t - t_o$. The black line and gray shaded area is for all *UT* (also shown in Figure 5c).

the 1 min used in Figure 5) because the higher time resolution is not needed and the 1-hr windows have fewer samples by a factor of roughly 24. The plot clearly shows that, on average, larger Φ_D is needed ahead of substorm onsets at 15–16 *UT* than is needed ahead of onsets at 02–03 *UT*. The difference between the two is roughly constant at about 4 kV at all negative values of $t - t_o$ shown and over that time this is a difference in opened flux of 0.058 GWb which is of order 10% of an average open polar cap flux, F_{PC} (Boakes et al., 2009; Milan et al., 2008).

At the start and end of the period shown Φ_D is 30 kV (4.9 kV above average) and starts to rise above this at $t - t_o$ near −150 min. Thus the contribution of enhanced magnetopause reconnection to the enhanced tail flux at onset, on average, begins at this time and increases until about 1 hr before onset (for the nominal propagation lag of $\delta t_p = 19$ min). It then reaches a plateau for about half an hour before rising to a peak at $t - t_o = -25$ min (for the nominal $\delta t_p = 19$ min). This marks the southward turning of the IMF that is usually taken to be the start of the growth phase. However, the plot reveals two levels of "preconditioning" by enhanced Φ_D before this time. The first is the 4.9 kV by which Φ_D is elevated above average values 4 hr ahead of onset. The second is the reconnection taking place in the 2 hr before the inferred southward turning (between $(t - t_o) = -150$ min and $(t - t_o) = -30$ min on average). Thus the open flux gained only between the southward turning and onset is not the only contribution to the tail lobe flux at the time of onset.

The first preconditioning, seen as the 4.9 kV by which Φ_D is elevated at $t - t_o = -240$ min appears at first sight that it might be a solar cycle effect; however, Figure 7 shows that this is not the case. Such an effect would arise if onsets were more frequent at higher solar activity, as one might expect, and so the long-term averages of Φ_D, *SMU*, and -*SML* would all be

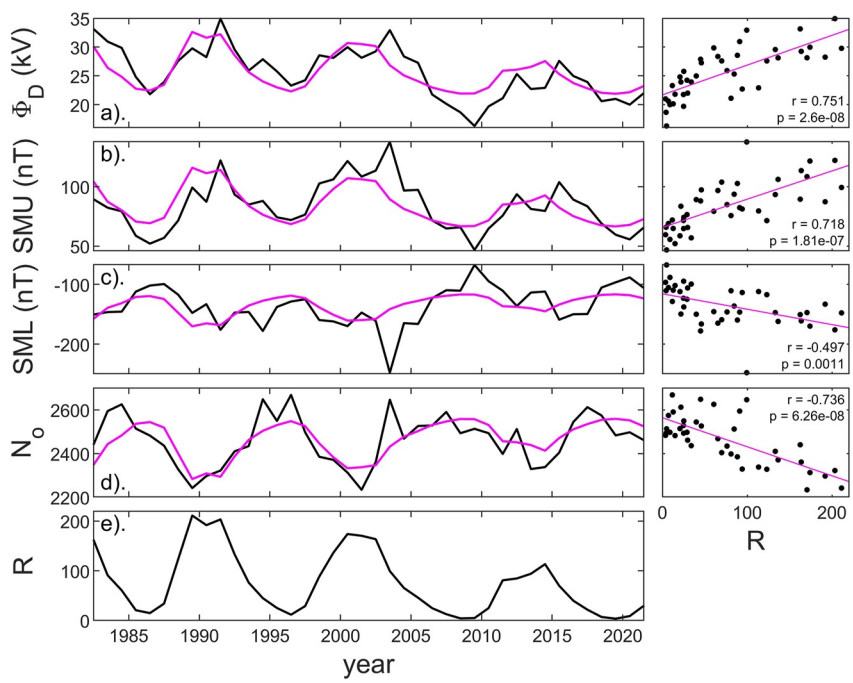

Figure 7. The left-hand column shows the Solar cycle variations in annual means (black lines) of: (a) the estimated magnetopause reconnection voltage, Φ_D; (b) the *SMU* index; (c) the *SML* index; (d) the number of substorm onsets, N_o; and (e) the international sunspot number, *R*. In panels (a–d) the mauve lines show the linear regression fit of *R* to the parameter. The right-hand column gives the scatter plots of the annual means with *R*, the mauve line being the linear regression fit. In each case, the correlation coefficient *r* and the *p*-value of the null hypothesis that there is no correlation are given.

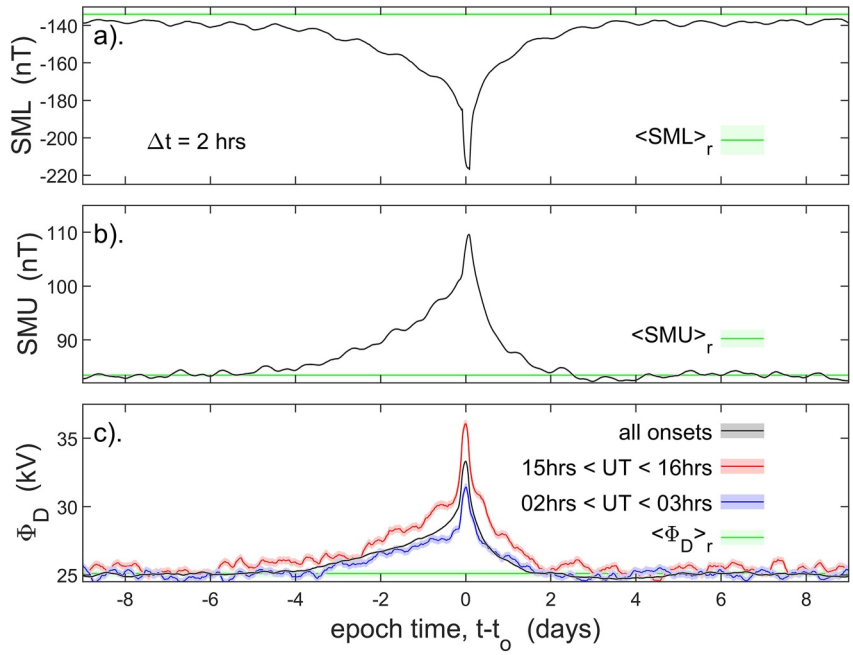

Figure 8. Super-posed epoch plots like those in Figures 5 and 6, but for integration intervals $\Delta t = 2$ hr and covering epoch times ($t - t_o$) between −9 days and +9 days, where t is the observation time and t_o is the time of onset, for: (a) the *SML* index; (b) the *SMU* index; and (c) the estimated reconnection voltage, Φ_D, lagged by a nominal propagation lag of $\delta t_p = 19$ min from the nose of the bow shock. The black lines are the means for all data and gray areas are plus and minus one standard error in the means. The green lines are for randomly selected epoch times. In Panel (c), the red and blue lines are means of Φ_D for onset *UT* between 15 and 16 hr (in red) and between 02 and 03 hr (in blue): the pink and pale blue shaded areas are plus and minus one standard error in the mean for these means.

increased above their overall means. Figure 7 plots the solar cycle variations in annual means for the data set used here (1985–2021) and although Φ_D, *SMU*, and -*SML* are all correlated with sunspot number *R* as we would expect, surprisingly, the number of onsets per year, N_o is anticorrelated with more onsets occurring at sunspot minimum. (Note that *SML* not -*SML* is plotted in Figure 7 and that the anticorrelation for *SML* is weaker than the other correlations (larger *p* value of the null hypothesis) largely because of the anomalous year 2003 for which the mean *SML* was exceptionally low).

On the anticorrelation of N_o and sunspot number, its notable that (Tanskanen et al., 2011) found that full substorm cycles were most common in the declining phase of the solar cycle: hence their study gave a phase lag (relative to the sunspot cycle) of about π/2 for the number of full substorm cycles whereas the present study finds a phase lag of near π for the number of substorm onsets. Milan et al. (2021) show that "driven convection" events occur when the dayside reconnection voltage Φ_D changes slowly enough for the nightside voltage Φ_N to respond and so the two can become balanced for extended periods in which no substorm cycles and no onsets occur. These events are what were termed "steady convection events" by Lockwood et al. (2009) and McWilliams et al. (2008) showed that they are considerably more common at sunspot maximum than at sunspot minimum. This could therefore offer an explanation of the anti-correlation of N_o and sunspot number. However, this may also be convolved with the effect of high-speed solar wind streams that are more common in the declining and minimum phase of the cycle and have been observed to generate High-Intensity Long-Duration Continuous AE Activity intervals in which substorm-like features merge into an interval of continuous substorm-like activity (Milan et al., 2023; Tsurutani et al., 2011): this could give more onsets at these cycle phases, as defined by the FEA and N&G algorithms.

Figure 7 shows that the enhanced Φ_D at the start of Figures 5 and 6 (over the overall mean value which is very close to the value for random selection of epoch times because the number of onsets is so high) is not due to the solar cycle variation in the numbers of onsets. Figure 8 looks at the origin of this by extending the interval covered by the superposed epoch study and including the plots for the random selection of epoch times (the green lines with pale green areas showing plus and minus one standard error; however, in most cases these are smaller

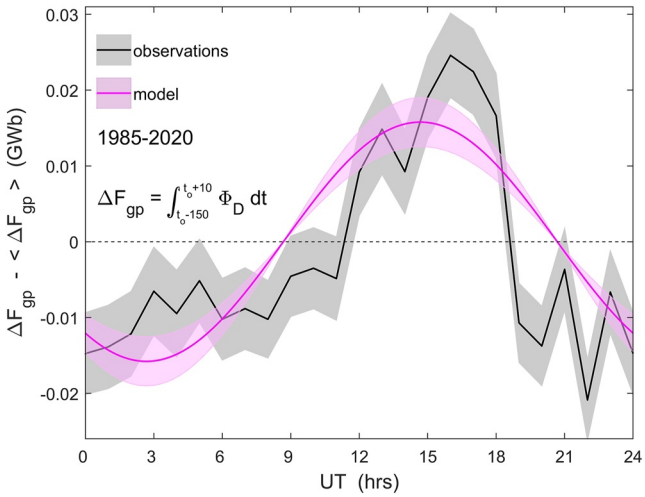

Figure 9. The variation of the open flux ΔF_{gp} generated in the substorm growth phase, taken to be the interval between 150 min before onset and 10 min after (using the nominal propagation lag of δt_p = 19 min from the nose of the bow shock), which is the integral of Φ_D over that interval. Values are shown as a function of *Universal Time* (*UT*) for 1-hr intervals of *UT* and with the mean for all *UT*, $\langle \Delta F_{gp} \rangle$, subtracted. The black lines are mean values from the data, with the gray area showing plus and minus one standard error in the mean. The mauve line is the model prediction (see Section 4 of text).

than the line width and not visible). In these plots the averaging interval was increased to Δt = 2 hr. Figure 8a shows that at epoch times well away from onset $(t - t_o) = -9$ days and $(t - t_o) = +9$ days, *SML* is very close to is overall mean and the randomly sampled value $\langle SML \rangle_r$. Figure 8b shows the same is true for *SMU*, the average vale being found at $(t - t_o) < -5$ days and $(t - t_o) > +2.5$ days. The black line in Figure 8c shows that Φ_D is the same as its randomly selected mean for $(t - t_o) < -5$ days and that the variation for 15–16 *UT* is not elevated above that for 02–03 *UT* for $(t - t_o) < -6$ days. Hence the *UT* variation in the voltage needed to cause an onset depends, to some degree, on a preconditioning (by prior magnetopause reconnection) of the substorm growth phase over an interval of about 6 days before the southward turning that traditionally marks the start of the growth phase. The average effect of that preconditioning can be seen to increase considerably after $(t - t_o) = -2.5$ days. Magnetopause reconnection is likely to continue after onset and only at $(t - t_o) > 2$ days does the mean value of Φ_D fall back to is overall mean value. Hence substorm onsets tend to sit in intervals about 4.5 days long in which Φ_D is enhanced over the overall mean value.

The persistence in the plots in Figure 8 is surprisingly large. It we take the e-folding times to decay to e^{-1} times away from the peak of Φ_D it is 0.99 days for going backwards with time before the peak and 0.42 days for after it. (For the 15–16 UT plot these e-folding times are 0.98 and 0.57 days, respectively, and for the 02–03 UT they are 1.11 and 0.46 days, and so very similar). Lockwood (2022) presented the autocorrelation functions for interplanetary parameters and for the various coupling functions derived from them. From these the correlation times (the e-folding times of the autocorrelation functions) are: 0.63 days for the flow-transverse component of the IMF $B_\perp$, 2.43 days for the solar wind speed, V_{SW}; 0.57 days for the solar wind mass density ρ_{SW}; and 0.07 days for the IMF orientation factor, $\sin^4(\theta/2)$ (where θ is the IMF clock angle in GSM). The value for Φ_D is 0.17 days. Hence the decays either side in the peak in Figure 8c are longer-lived than the autocorrelation time of the Φ_D data series. However, Figure 8 is showing the average of a great many cases. If we look at the variations around individual onsets at high time resolution they show frequent falls to near-zero Φ_D and then recoveries on typical variation timescale of about 0.05–0.1 days caused by the great variability in the IMF orientation factor. The greater persistence in the average of Φ_D for many cases arises because the variability in the IMF orientation factor averages out to a near constant factor and we see the greater persistence of the other parameters that contribute to Φ_D (in particular, the solar wind speed V_{SW}). Hence it is the relative longevity of the more-geoeffective fast solar wind streams that give the great persistence in the averages shown by the superposed epoch plots for Φ_D, *SML*, and *SMU* in Figure 8.

It is interesting to note that integrating Φ_D over the interval between the apparent southward turning of the IMF (at $(t - t_o) = -35$ min, when mean values of Φ_D start to rise sharply to the pre-onset peak) and $(t - t_o) = 10$ min, we find a total of 0.3 GWb of open flux is generated. If we look at the total opened over the preconditioning interval -4 days $< (t - t_o) < -35$ min, it is 9.3 GWb. Much of this open flux will be lost and Figure 8a shows that average -*SML* increases with the increasing Φ_D over this interval, indicating enhanced open flux loss by enhanced nightside reconnection. However it is interesting how little open flux is, on average, generated in the growth phase and how much the occurrence of a substorm onset relies on open flux accumulated during the preconditioning phase. The growth phase adds the final flux that triggers onset, but the role of prior open flux and preconditioning appears to be very significant.

3.1. *UT* Variations in the Reconnection Voltage Φ_D Prior to Onset

The black line in Figure 9 shows the variation of mean open flux generated in the interval 150 min before onset to 10 min after, ΔF_{gp}, evaluated in bins of *UT* that are 1 hr wide. This is surrounded by a gray area that is plus and minus one standard error in these means. Because the variations of average Φ_D with elapsed time $(t - t_o)$ are very similar in form for all *UT*s (as in Figure 6), the results are insensitive to the interval of elapsed times that is adopted. Indeed, the same form is even seen if we take the integral over the whole preconditioning interval

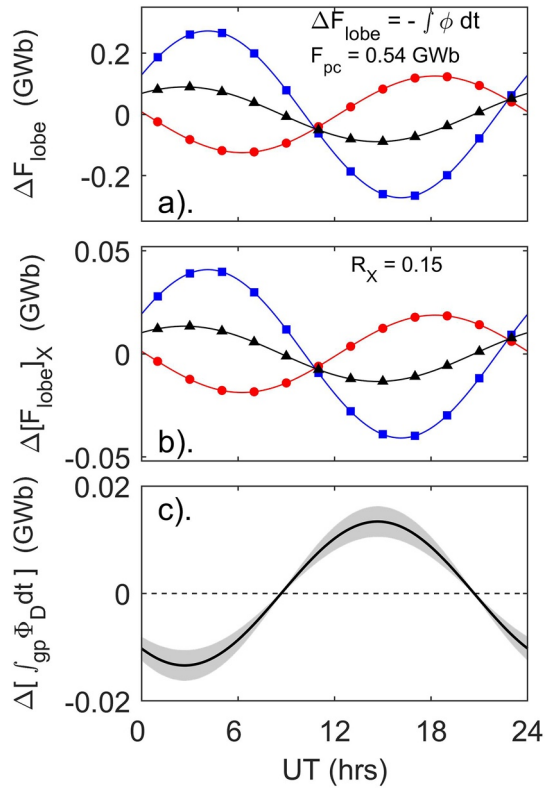

Figure 10. Variations giving the model prediction of the *UT* variation of flux opened during the growth phase, ΔF_{gp} shown in Figure 9. (a) The flux added to the lobes by the pole motions, ΔF_{lobe}, shown using the same colors and symbols as in Figure 3 (namely: red lines with red circle symbols are for the northern hemisphere polar cap, blue lines with blue square symbols are for the southern hemisphere polar cap and black lines with triangle symbols are for the global average of the two). This is the integral of ϕ with time for an average polar cap flux of F_{PC} of 0.54 GWb (giving a polar cap diameter d_{PC} of 3.73×10^6 m). (b) The variation in $[F_{lobe}]_X$, at a X coordinate of the tail reconnection site ($X = -21\ R_E$) (the same as inferred from the numerical simulation shown in Figure 1 and described below in Section 5). The value of R_X is 0.15, also used to make the model predictions in Figure 4. (c). The variation in the integrated growth phase reconnection voltage needed to offset the variation in the average tail $[F_{lobe}]_X$ caused by pole motions. This is an inversion of the black line in panel (b). The uncertainty band shown in gray is derived in Section 5.

of 4 days before onset, as discussed above; however, just as the total fluxes opened in that longer interval are roughly 30 times larger than in the hour before onset (as discussed in the previous section), so the amplitude of the *UT* variation is also 30 times larger.

This plot shows that there is a significant *UT* variation in the flux that is opened ahead of substorm onsets. The mauve line (with an estimated error shown by the pink area) is the predicted variation for pole motion effect. This uses a value of R_X of 0.15 in both hemispheres and was derived in Section 4 using the model used to predict the onset occurrence (see Figure 4a) and described in Section 2.1. The uncertainty of ±20% that is derived in Section 5 from the numerical model predictions shown in Figure 1. It can be seen that this model prediction is not matching all the detail of the observed variation, but both the phase and the amplitude of the main component is well reproduced. Hence the *UT* variations in both the occurrence of onset and the integrated reconnection voltage needed to trigger a substorm can be predicted by the model based on the effect of pole motions.

4. Analysis of *UT* Variation of Flux Added in Substorm Growth Phase

Figure 10a gives the changes in the lobe fluxes (at X near zero) caused by the motions of the poles, ΔF_{lobe}. This is the integral of the pole motion voltage ϕ with time. The colors and symbols are as used in Figure 3. Figure 10b is the variation of the lobe flux at $X = -21\ R_E$, $\Delta[F_{lobe}]_X$, obtained by multiplying the variations in Figure 10a by $R_X = 0.15$. The justification for this factor is discussed in the next section. The black line is the average of the two which will be half the *UT* variation of the total lobe flux in the tail, $\Delta[F_{tail}]_X$. The model assumes that it is this total flux that sets the probability of substorm onset occurring. To compensate for the *UT* variation in $\Delta[F_{tail}]_X$ and give the same probability of onset requires a *UT* variation in the total open flux produced by magnetopause reconnection which is given by the black line in Figure 10c. This is the same variation as the black line in Figure 10b, but inverted: it is the integral of the magnetopause reconnection voltage Φ_D needed, which has been derived from the superposed epoch analysis of the data in Section 3.1. The uncertainty band shown by the gray area is for a ±20% variation in R_X which is derived in the next Section 5.

The variation shown in Figure 10c is reproduced in Figure 9 as the mauve line with the uncertainty plotted in pink. It can be seen that the model is reproducing main phase and amplitude of the variation in prior reconnected flux with *UT*. The amplitude depends on value of R_X of 0.15 which agrees with the simple Monte-Carlo model of onset occurrence and which, in the next section, is found to be a reasonable value using the numerical simulations which gave Figure 1.

5. Numerical Modeling of the Magnetotail Response to Dipole Tilt

This section uses the results of a numerical, global, MHD model of the magnetosphere, shown in Figure 1, to gain some understanding of the factors R_{SX} and R_{NX} in Equation 8. The simulations are made using the BATS-RUS global numerical model of the magnetosphere, specifically Space Weather Modeling Framework (SWMF) version v20140611 which deploys the Rice Convection Model. The runs were performed using NASA's Community Coordinated Modeling Center (CCMC) (Tóth et al., 2005) and the simulation results are described in the data availability section and were those used by Lockwood, Owens, Barnard, Watt, et al. (2020).

The simulations used are for tilt angles δ of 0, 34° and −34°. (Note that the use of a geocentric dipole field means that the third simulation for $\delta = -34°$ gave identical results to $\delta = +34°$ but with the north and south hemispheres

reversed). All three simulations were started (at simulation time $t_s = 0$) with a large open flux of $F_{PC} = 0.85$ GWb which decayed until near steady state was achieved shortly after $t_s = 90$ min. The decay was greater for $\delta = \pm 34°$ than for $\delta = 0$ largely because the dayside reconnection voltage Φ_D was persistently lower for $\delta = \pm 34°$ and the nightside loss rate was high in both cases because F_{PC} was high. At simulation time $t_s = 90$ min, F_{PC} was 0.583 GWb for $\delta = 0$ and 0.509 GWb for $\delta = \pm 34°$, a ratio of 1.145. For this time, the numerical simulations give Φ_D of 90.8 kV for $\delta = 0$ and 78.3 kV for $\delta = \pm 34°$. These voltages were computed from the MHD simulation results using a variant of the method described by Laitinen et al. (2006). Specifically, the magnetopause location was defined from the abrupt change in plasma β and field lines at grid points on either side of this boundary traced in both directions using the tracing derived by the model. Field lines are then classified as A. disconnected (interplanetary only), B. open and connected to the south pole ionosphere, C. open and connected to the north pole ionosphere or D. closed (both ends connected to the ionosphere). Points between category B and C field lines and between category A and D field lines were identified as close to the reconnection X-line which was defined as the average of the midpoints between the pairs of opposing categories. These locations were then connected using Piecewise Cubic Hermite Interpolating Polynomial (PCHIP) interpolation of their X, Y, and Z GSE coordinates and the electric field variation along this X-line also derived by PCHIP interpolation of nearby grid point values. When integrated along the X-line, these interpolated electric field (reconnection rate) values yield an estimate of Φ_D at that time.

The ratio of the reconnection voltages in the two cases was 1.160, similar to the ratio for F_{PC}. To allow for the different reconnection rates and make comparisons, all open magnetic fluxes are adjusted so that the F_{PC} is the average of the $\delta = 34°$ and $\delta = 0$ cases (i.e., 0.546 GWb) which means multiplying the open flux for $\delta = 0$ by 0.937 and that for $\delta = \pm 34°$ by 1.073. We also apply these factors to the two parts that add up to the total open flux (Equation 4), F_X and $[F_{lobe}]_X$. The analysis was repeated without these flux normalization factors and the results for R_X were very similar because their effects on the fluxes F_X, ΔF_{PM}, and F_{PC} are very similar. As well as using the mean of the open flux for $\delta = 0$ and $\delta = 34°$, the value for each was employed and used to set an uncertainty on the R_X values derived.

The input solar wind parameters in the simulations were held constant and were solar wind speed $V_{SW} = 400$ km s^{-1}, solar wind number density $N_{SW} = 3 \times 10^6$ m^{-3}, mean ion mass $m_{SW} = 1.1$ amu, IMF flow-transverse component $B_t = 5$ nT and an IMF clock angle in GSM $\theta = 180°$. Note that the dayside reconnection voltages of 90.8 and 74.3 kV generated by the model are both larger than we would expect from these input solar wind parameters using the empirical relationship by Lockwood and McWilliams (2021a) which gives 56.1 kV for Φ_D but are more similar to the total polar cap voltage Φ_{PC} from the same study (which includes the effect of nightside reconnection and any viscous-like voltage) of 69.6 kV.

Figure 1 gives an indication of how dipole tilt effects influence the magnetosphere but it is not the whole story as it only shows the (XZ) plane at $Y = 0$ and does not reveal the behavior closer to the dawn and dusk flanks. Figure 11 uses the same simulations to show how the total flux in the tail can be computed. It shows the magnetic field B in cross sections of the tail (YZ planes at various X) in which the minima in B clearly reveal the locations of the magnetopause currents and the cross tail current separating the lobes. (Both are also clearly identified from the simulated currents). The middle panel is for dipole tilt $\delta = 0$ and the two lobes are symmetrical at all times and the cross-tail current lies at $Z = 0$ at all X and Y.

The left-hand panel shows that for dipole tilt angle $\delta = +34°$ the cross tail current sheet is warped, such that its displacement to positive Z seen at $Y = 0$ in parts a and c of Figure 1 is a maximum but this displacement in Z is close to zero at the dawn and dusk flank of the tail where it connects to the magnetopause currents. It can be seen that for $\delta = +34°$ the field in the southern lobe is considerably enhanced at all X compared to the $\delta = 0$ case, whereas in the northern hemisphere it is decreased. Because this simulation is for an geocentric dipole field, the southern hemisphere for $\delta = +34°$ is identical to the northern hemisphere for $\delta = -34°$ (Lockwood, Owens, Barnard, Watt, et al., 2020).

For both values of δ, the field in the tail decreases with increasingly negative X. From the integral of the field threading the cross sections of the tail (the B_X component) we obtain the magnetic flux in each lobe at each X, $[F_{lobe}]_X$. At X below about $-20\ R_E$ there is no closed flux in the tail and so the decrease in this flux with increasingly negative X is only because of open flux F_X that threads the magnetopause sunward of the X in question.

From Equation 4 we can compute the flux threading the magnetopause sunward of X, F_X and this is shown as a function of X in Figure 12a for the northern hemisphere for dipole tilt angles (positive for northern hemisphere tipped towards the Sun) of (red) $\delta = +34°$, (green) $\delta = 0$, and (blue) $\delta = -34°$. This plot shows that the magnitude

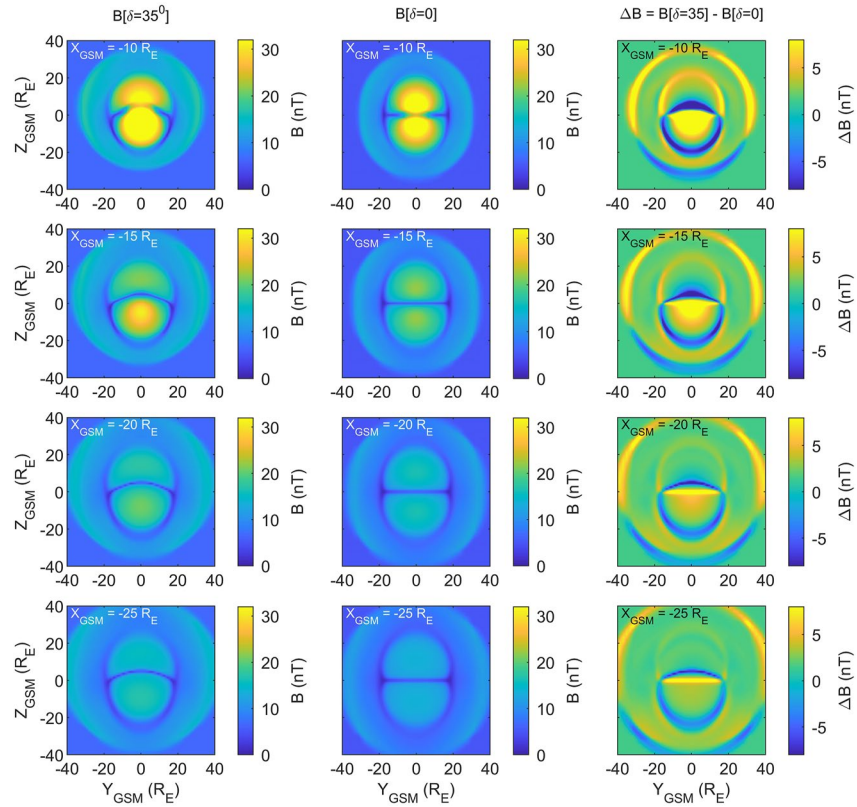

Figure 11. Cross-sections of the tail showing the field strength B in the GSM YZ plane from the simulations shown in Figure 1. From top to bottom the rows are for X of −10, −15, −20, and −25 R_E. The left-hand column is for dipole tilt angle $\delta = +34°$, the middle column is for $\delta = 0$ and the right-hand column shows the difference between the two, ΔB.

of the effect on F_X for a hemisphere tilted towards the Sun is somewhat smaller than for a tilt of the same magnitude away from the Sun. Hence the variation in the tail is not linear with δ.

From these variations we can compute the R_X factors. By integration of the definition of R_X with time, we have:

$$R_X = (dF_X/dt)/\phi = F_X/\int \phi dt = F_X/F_{PM} = \Delta F_X/\Delta F_{PM} \quad (9)$$

where in this case we consider the deviation from the $\delta = 0$ case, $\Delta F_X = [F_X]_\delta - [F_X]_{\delta=0}$. The corresponding flux ΔF_{PM} is given by $d_{PC}.B_i.\Delta X$ where ΔX is the difference in the X coordinate of the diameter of the polar cap for tilt angles of δ and of $\delta = 0$. This yields $|\Delta F_{PM}|$ of 0.585 GWb for the 34° change in δ. The red lines in Figure 12b gives the values of R_X for tilting the polar cap sunward from $\delta = 0$ to $\delta = +34°$ (or antisuward the other way) and the blue line the value of R_X for tilting the polar cap sunward from $\delta = -34°$ to $\delta = 0$ (or, again, antisuward the other way). The black line gives the average over a whole year of R_X for the daily sunward/antisunward motion, $\langle R_X \rangle_{1yr}$. The derivation of this from the simulation results is explained by Figure 13.

Figure 13 is for the example X of −21 R_E. The points in Figure 13a are the values of the flux threading the dayside magnetopause F_X for $\delta = +34°$, $\delta = 0$, and $\delta = -34°$ at this X, as given in Figure 12a. The line is a second order polynomial fit to these points. This has been extended out to ±39°, which is the full range of possible δ values that the south pole can have. The vertical dashed lines mark the range of the annual variation due to Earth's orbital motion (±23.44°). For each value of δ between the dashed lines, the diurnal variation in δ is added and the diurnal change in F_X (ΔF_X) that it causes is then scaled from the polynomial fit in Figure 12a and the corresponding change in the pole motion flux F_{PM} (ΔF_{PM}) (the integral of ϕ calculated from Equation 1): ΔF_X and ΔF_{PM} are shown in Figures 12b and 12c, respectively, as a function of the daily mean δ, and the ratio of the two, (equal to R_X by Equation 9), is shown in Figure 12d.

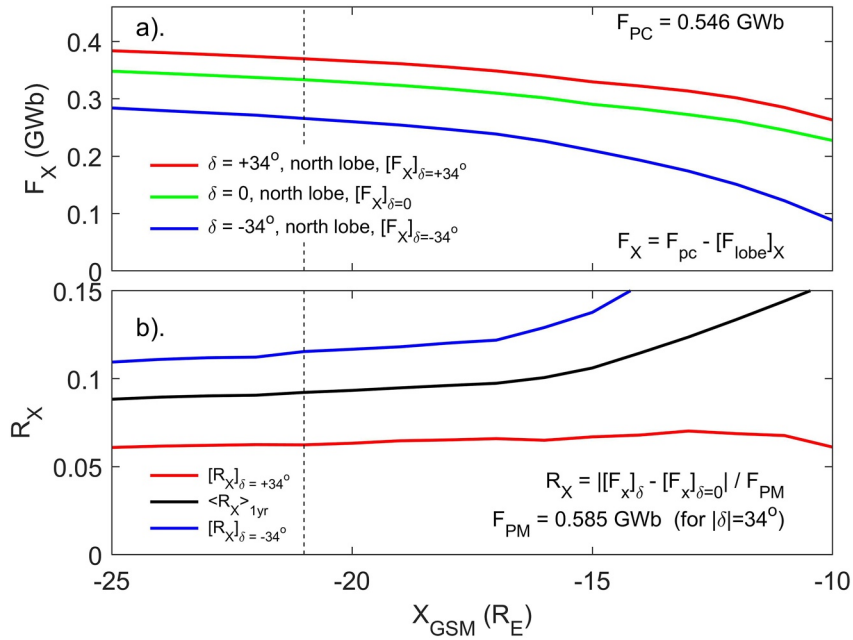

Figure 12. (a) Variation of the fluxes threading the dayside magnetopause F_X with X for a fixed polar cap flux F_{PC} of 0.546 GWb: red, green, and blue are for dipole tilt angles (positive for northern hemisphere tipped toward the Sun) of $\delta = +34°$, $\delta = 0$, and $\delta = -34°$. The X of the tail reconnection site ($-21\ R_E$) is shown by the vertical dashed line. (b) The values of R_X derived from panel (a) for (red) $\delta = +34°$ and (blue) $\delta = -34°$. The black line is the annual mean of the R_X values that are due to diurnal motions, $\langle R_X \rangle_{1yr}$, the derivation of which is explained in Figure 13.

A total of 365 values of R_X were computed for the daily average of δ of each day of the year and the mean taken to give the average value over a full year caused by the diurnal variation. The results show the means are the same for the two hemispheres and equal to 0.092. The analysis was re-run using the F_{PC} of the $\delta = +34°$ simulation and then again using that for $\delta = 0$ (rather than the mean of the two which is used in Figures 12 and 13). This yields an uncertainty range in the R_X value of ± 0.013.

The R_X value of 0.092 is of the required order of magnitude but is smaller than the 0.15 used in Figure 9, and we need to look for potential missing factors of the ratio of the two, 1.6. There are a number of considerations that can, individually or collectively, explain this factor. The values of R_X depend on how much recently opened flux is present and so the time history of Φ_D is important: larger fluxes of more-recent opened field lines give a higher F_X for a given F_{PM}. The simulations are for near constant Φ_D whereas in substorm growth phases Φ_D has increased with time, giving a higher fraction F_X/F_{PC}. However, from the time variations of Φ_D shown in Figure 5, this factor gives, at most, a rise by a factor of only about 1.05 in R_X. A bigger factor is the value of the open flux F_{PC} which is only 0.546 GWb in the simulations but Boakes et al. (2009) find is typically 0.75–0.9 at the time of onset. The value of F_X is close to being proportional to F_{PC} and, for a circular polar cap, ϕ (and hence F_{PM}) is proportional to $F_{PC}^{0.5}$. Hence, by Equation 9, R_X is proportional to $F_{PC}^{0.5}$. This gives a factor of between 1.2 and 1.3. Another factor is the number density of the solar wind, N_{SW} which controls the magnetosheath density at the dayside magnetopause, and hence the Alfvén speed with which newly opened field lines move over the dayside magnetopause away from the reconnection site. In the simulation, a low value was used (3×10^6 m^3) whereas the average value is roughly twice this. Increasing N_{SW} by a factor of 2 would lower the Alfvén speed at the dayside magnetopause by a factor of $2^{0.5} = 1.4$ and this would increase the F_X for a given F_{PC} and δ. This would therefore also increase the R_X. Lastly, the value of $R_X = 0.092$ is derived from the simulations for the reconnection X-line position in those simulations at the steady state achieved at simulation time $t_s = 90$ min. As shown in Figure 1, this is at $X = -21 R_E$. It is highly probable that the X-line at substorm onset forms closer to the Earth than this and Figure 12 shows that the simulations give $R_X = 0.11$ at $X = -15\ R_E$ and $R_X = 0.12$ at $X = -13\ R_E$.

These considerations mean that the simulations can only be used as an order of magnitude guide but we can conclude that they give R_X values that are reasonably consistent with the empirically derived value of 0.15, particularly if we take all the factors that are likely to increase the value of R_X into account.

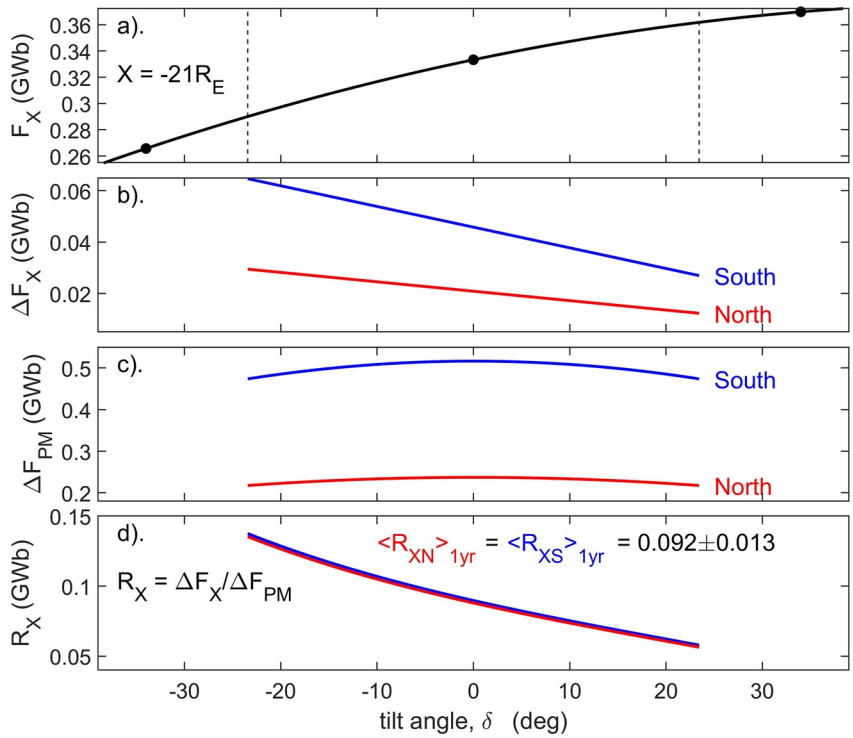

Figure 13. The derivation of the annual mean of the R_X values due to diurnal motions, $\langle R_X \rangle_{1yr}$ (the black line in Figure 12b) shown here for the example X of -21 R_E. The points in panel (a) are the values of the fluxes threading the dayside magnetopause F_X for $\delta = +34°$, $\delta = 0$, and $\delta = -34°$, as given in Figure 12a and the line is a second order polynomial fit to these points. The plot covers the full potential range of δ (for the southern pole) and the vertical dashed lines mark the range of the annual variation due to Earth's orbital motion. For each value of δ in this range the maximum and minimum δ due to the diurnal variation is considered and the change that the diurnal motions cause in F_X, ΔF_X is scaled from the polynomial fit in panel (a) and shown in panel (b) as a function of the daily mean of δ. The corresponding change in the pole motion flux caused by the diurnal motion in the polar cap (the integral of ϕ) is calculated from Equation 1, ΔF_{PM}, and shown in panel (c). Panel (d) gives $R_X = \Delta F_X/\Delta F_{PM}$. The mean value over a whole year for both hemispheres is 0.092. An uncertainty is derived using the open flux for each of the two runs, rather than the mean of the two. This yields an uncertainty in the change that the diurnal motions cause in R_X of ± 0.013.

6. Discussion and Conclusions

This paper has studied systematic *UT* variations in magnetospheric substorms, using a simple Monte-Carlo model and 1-min observations taken over a 34-year interval. In addition, a global numerical MHD model has been used to show that simulated tilt-induced changes in tail lobe flux at the tail reconnection site are of the magnitude expected for this effect. Note that the MHD model used cannot reproduce the net pole-motion effect directly because it uses a geocentric rather than an eccentric dipole model of the geomagnetic field. All reveal an effect consistent with the effect of diurnal motions of the magnetic poles in a geocentric-solar frame of reference caused by Earth's rotation and the eccentric dipole nature of the intrinsic geomagnetic field.

The analysis has focused on the effect of dipole tilt on the tail flux as an explanation of *UT* effects but we should also remember that the num,erical simulations give a dayside reconnection voltage Φ_D that is 16% higher (92 kV) for $\delta = 0$ than for $\delta = \pm 34°$ (78 kV). As discussed in Section 1.6 such a variation in Φ_D with δ has been invoked as the origin of the equinoctial pattern and we need to be clear what this means for average variations with *UT*. By Maxwell's equation $\nabla . \vec{B} = 0$, Φ_D must be the same for both hemispheres (as must Φ_N) but note that transpolar voltages Φ_{PC} can differ in the two polar caps because of induction effects associated with field changes in the magnetosphere and magnetosheath. For simplicity of explanation, we here consider a geocentric dipole (epoch 2003) and the fact that Φ_D must be the same for the two hemispheres means that the variation of Φ_D with δ must be symmetrical about zero, such that the value for a given tilt δ is the same as that for $-\delta$. The left hand column in Figure 14 shows four model variations of Φ_D with δ that meet this condition. In row (**A**) there is a minimum in Φ_D at $\delta = 0$. The right hand panel shows the *F-UT* pattern of Φ_D (*F* being the fraction of a calendar year) that

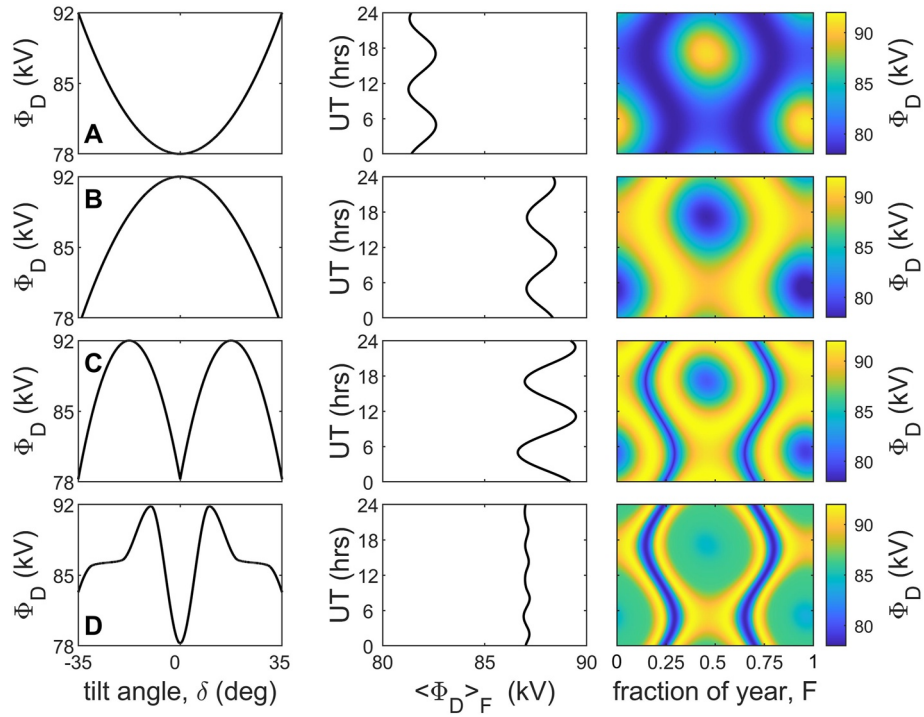

Figure 14. Analysis of the effects of various variations of the magnetopause reconnection voltage, Φ_D, with the tilt angle δ. The left-hand column gives the variation of Φ_D with δ. The right-have column gives the resulting *F-UT* pattern of Φ_D (where *F* is the fraction of a calendar year). The middle column gives Φ_D averaged over a year (*x*-axis) as a function of *UT* (*y*-axis). The input variations are all scaled between a maximum of 92 kV and a minimum of 78 kV to match the results of the numerical MHD simulations shown in Figures 1, 11, and 12 and a geocentric dipole is used for simplicity. The top row (a) is for a minimum Φ_D at $\delta = 0$; row (b) is for a maximum at $\delta = 0$ (the variation consistent with the numerical simulation results) row (c) is for a maxima at $|\delta| = 17.5°$ and row (d) is the variation from the numerical simulations by Eggington et al. (2020) (scaled to the same minimum-to-maximum range as the other panels).

this generates. Averaging over all 365 days of a year at a given *UT* yields the means $\langle \Phi_D \rangle_F$ shown as a function of *UT* in the middle panel the middle panel. The *F-UT* pattern is an "inverse equinoctial" pattern: inverse because the contours of low $|\delta|$ give minima. The variation with *UT* shows a semi-diurnal form with minima near 11 and 23 *UT*.

Row (**B**) shows the case for a maximum in Φ_D at $\delta = 0$. This is the case that was revealed by the numerical simulations discussed in Section 5 and, indeed, the variation has been scaled to the values obtained in that section for $|\delta| = 0$ and $|\delta| = \pm 34°$. This does give the equinoctial pattern, with low $|\delta|$ giving maxima, as seen for geomagnetic activity. The *UT* variation again has a semi-diurnal form, but this time it is maxima at 11 hr *UT* and 23 hr *UT*.

Row (**C**) shows what happens when the peak Φ_D is at an intermediate δ (here $\pm 17.5°$). The *F-UT* pattern is like an equinoctial form but is more complex, having a deep minimum embedded within the bands of the maximum Φ_D. The *UT* variation is, however, the same in form as for (**B**).

The global numerical simulations by Eggington et al. (2020) are of great relevance to the present study. These authors increase the tilt angle up to the extreme limit of 90° but we here consider only the range 0°–34° applicable to the Earth. Figure 7a of that paper shows that the simulated magnetopause reconnection voltage Φ_D increases with increased tilt angle between about 0 and 10° but thereafter decreases. Figure S2 of the Supporting Information file accompanying the paper by Eggington et al. (2020) shows that the open flux decreases with increased tilt angle. This means that the change in the tail reconnection voltage Φ_N is not the same as that in Φ_D and the tail voltage is independently influenced by the tilt angle, as is inferred in the present paper. The imbalance of Φ_N and Φ_D means that the magnetosphere-ionosphere system is not in steady state (Cowley & Lockwood, 1992), something that can also be seen in their Figure 7b which shows unequal voltages across the northern and southern ionospheric polar caps.

Row (**D**) shows the results for the variation of Φ_D with δ from the simulation results of Eggington et al. (2020). These have been scaled up to the same range as the other variations in the figure. At first sight we would expect the results to be similar to those in row (**C**) for peak Φ_D at intermediate δ and indeed, the *F-UT* plot has similarities but the features are much narrower and sharper. This has a major effect when we average over all *F* and no consistent variation of $\langle\Phi_D\rangle_F$ with *UT* is seen. However, it should be noted that the simulations by Eggington et al. (2020) show considerable rapid time variation in Φ_D which the authors smooth by taking 5-min averages with the variation indicated by error bars. This variability may have influenced the Φ_D variation with δ that is here taken from the smoothed averages and hence differences between row (**D**) and row (**C**) of Figure 14 may not be significant. Indeed the decrease in Φ_D at δ below 10° may not be significant considering this numerical noise in which case the difference between rows (**D**) and (**B**) are not significant. In this case the study by Eggington et al. (2020) can be considered to give a dipole tilt dependence that could, potentially, explain the equinoctial pattern through the modulation of the magnetopause reconnection voltage, Φ_D. However, as discussed earlier, a key point about these simulations is that the open flux decreases with tilt angle meaning that the reconnection voltage in the cross tail current sheet Φ_N decreases by more than the decrease in Φ_D. This points to a second, larger and independent mechanism decreasing Φ_N with increased tilt angle and explaining the equinoctial pattern. This is consistent with the findings of empirical studies (Finch et al., 2008; Lockwood, Owens, Barnard, Haines, et al., 2020; Lockwood, Owens, Barnard, Watt, et al., 2020) and numerical modeling studies presented here and by Lockwood, Owens, Barnard, Watt, et al. (2020).

Figure 14 shows that variations of Φ_D with δ can give an equinoctial pattern but the diurnal variation seen when data for a given *UT* are averaged over all *F* gives two peaks a day. These are at 10.8 hr *UT* and 22.8 hr *UT* for a geocentric dipole and at 9.0 hr *UT* and 21.0 hr *UT* for an eccentric dipole (times for 2003). Figure 9 shows the dominant variation is diurnal and not semidiurnal which eliminates variations in the magnetopause reconnection rate as the cause. That being said, the deviations from a pure sinusoidal form in Figure 9 might well be explained by a semi-diurnal oscillation in Φ_D, but that would be a considerably smaller amplitude modulation than the dominant diurnal one shown.

Another reason why we can discount the effects of modulation of Φ_D by δ for the effects studied here comes from the superposed epoch plots shown on Figure 8c. If the difference between the variations at a given *UT* were due to semi-diurnal variations in Φ_D, we would expect the superposed epoch variations to show oscillations in Φ_D with a 1-day period. These are not seen, but can be seen in the plots for *SML* and *SMU* (Figures 8a and 8b), which we would expect because of conductivity effects. We do note, however, that tilt angle effects on Φ_D could give the equinoctial pattern, but the evidence points to a larger tilt angle effect on the nightside reconnection voltage Φ_N, be it through enhanced instability in the tail to substorm onset, that is, through lowering the tail flux threshold needed for onset to occur—as proposed by Kivelson and Hughes (1990), or through the effect of dipole tilt on the tail field, as modeled by Lockwood, Owens, Barnard, Watt, et al. (2020).

On the other hand, the paper has shown that the *UT* variations are consistent with the diurnal pole motions of an eccentric dipole. Using a simple Monte-Carlo model based on the idea that the probability of onset is raised by the total magnetic flux in both lobes in the near-Earth tail, we can model the observed *UT* variation in the number of onsets (Figure 4) except the model as yet has no way of including recurrent substorms due to persistent southward IMF and instead re-starts each growth phase at a random time.

This idea (of the probability of substorm onset being raised by the tail lobe field which is modulated by the dipole tilt) is supported by the superposed epoch studies. These clearly show larger magnetopause reconnection voltages are required for onsets at some *UT*s than at others. Figure 8 shows that the average behavior is that after a substorm onset the reconnection voltage has fallen back to it average value in about 2 days. However, before onset a considerably longer period of enhanced opening of magnetospheric flux is required. The plots (Figures 5 and 8) reveal a rise in Φ_D, on average, of order 30 min ahead on an onset. This is consistent with the southward turning that traditionally starts substorm growth phases. However there seems to be two levels of preconditioning before this. The first is an average rise in Φ_D in the 100 min prior to the southward turning. The second is a preconditioning from overall average levels that increases over the prior 6 days. Analysis of solar cycles shows, somewhat surprisingly, substorm onsets are more common at sunspot minimum and hence this cannot be attributed to the variation of average solar wind conditions with the sunspot cycle.

A theory that allows us to accommodate the effect of pole motions and an eccentric dipole into magnetospheric dynamics has been presented. In relation to substorm growth phase termination and onsets, the major unknown

is the extent to which dipole tilts influence the tail and X coordinates that influence onset. This has been allowed for in the present paper with the factor R_X, which is the ratio of the change in tail lobe flux at the X coordinate of the tail reconnection site to the change in total open flux in that lobe (Equations 5 and 6). The Monte-Carlo model of onsets requires $R_X \approx 0.15$, a value that is shown here to agree well with the UT variation found from the superposed epoch studies. A test of this value using a numerical MHD model of the magnetosphere is shown to result in a value near 0.10. However, there are a number of factors that could be invoked to increase this number and make it consistent with the 0.15 value. The present paper does no more than establish that the numerical model simulations show an effect that gives the required diurnal variation with the correct phase, but the amplitude is smaller than needed to fit the observations by a factor of about a third. Further work is needed to establish if indeed $R_X = 0.15$ is the correct value.

Data Availability Statement

The data used in this study are all openly available. The interplanetary data are available from the Physics Data Facility (SPDF) at NASA's Goddard Space Flight Center as the Omni composite from https://omniweb.gsfc.nasa.gov/ow_min.html. The SuperMAG SML and SMU indices and the substorm onset lists are available from the SuperMAG project website at the Johns Hopkins University Applied Physics Laboratory at http://supermag.jhuapl.edu/indices/. The numerical MHD model results are available from NASA's Community Coordinated Modeling Center (CCMC) and the simulation results are available from https://ccmc.gsfc.nasa.gov. The results are from the BATSRUS global numerical model of the magnetosphere, specifically Space Weather Modeling Framework (SWMF) version v20140611 which deploys the Rice Convection Model. The runs employed are labeled $Henry_Z hou_0 40616_1$, $Henry_Z hou_0 40616_2$, $Henry_Z hou_0 40616_3$).

Acknowledgments
The author is grateful to the many instrument scientists and engineers who make the data sets employed in this study possible and the staff of a number of datacentres who allow easy access to the data: in particular the Space Physics Data Facility (SPDF) at NASA's Goddard Space Flight Center for the Omni composite of interplanetary observations and the SuperMAG project staff coordinated at The Johns Hopkins University Applied Physics Laboratory, for the SMR and SML indices. The author thanks the many PIs and instrument teams who contribute data to the SuperMAG project. The global MHD simulation results were obtained using BATSRUS, developed by the Center for Space Environment Modeling, at the University of Michigan with funding support from NASA ESS, NASA ESTO-CT, NSF KDI, and DoD MURI. The author also thanks the staff on NASA's Community Coordinated Modeling Center (CCMC) for making access to and exploitation of the model simulations possible, This work is supported by a number of Grants: consolidated Grants ST/R000921/1 and ST/V000497/1 from the United Kingdom Science and Technology Facilities Council (UKRI/STFC) and the SWIGS Directed Highlight Topic Grants NE/P016928/1 and NE/S010033/1 from the United Kingdom Natural Environment Research Council (UKRI/NERC).

References

Alexeev, I. I., Belenkaya, E. S., Kalegaev, V. V., Feldstein, Y. I., & Grafe, A. (1996). Magnetic storms and magnetotail currents. *Journal of Geophysical Research*, *101*(A4), 7737–7747. https://doi.org/10.1029/95JA03509

Bartels, J. (1936). The eccentric dipole approximating the Earth's magnetic field. *Journal of Geophysical Research*, *41*(3), 225–250. https://doi.org/10.1029/TE041i003p00225

Berthelier, A. (1976). Influence of the polarity of the interplanetary magnetic field on the annual and the diurnal variations of magnetic activity. *Journal of Geophysical Research*, *81*(25), 4546–4552. https://doi.org/10.1029/JA081i025p04546

Boakes, P. D., Milan, S. E., Abel, G. A., Freeman, M. P., Chisham, G., & Hubert, B. (2009). A statistical study of the open magnetic flux content of the magnetosphere at the time of substorm onset. *Geophysical Research Letters*, *36*(4), L04105. https://doi.org/10.1029/2008GL037059

Boyle, C. B., Reiff, P. H., & Hairston, M. R. (1997). Empirical polar cap potentials. *Journal of Geophysical Research*, *102*(A1), 111–125. https://doi.org/10.1029/96JA01742

Brekke, A., & Moen, J. (1993). Observations of high latitude ionospheric conductances. *Journal of Atmospheric and Terrestrial Physics*, *55*(11–12), 1493–1512. https://doi.org/10.1016/0021-9169(93)90126-J

Carter, J. A., Milan, S. E., Paxton, L. J., Anderson, B. J., & Gjerloev, J. (2020). Height-integrated ionospheric conductances parameterized by interplanetary magnetic field and substorm phase. *Journal of Geophysical Research: Space Physics*, *125*(10), e2020JA028121. https://doi.org/10.1029/2020JA028121

Cliver, E. W., Kamide, Y., & Ling, A. G. (2000). Mountains versus valleys: Semiannual variation of geomagnetic activity. *Journal of Geophysical Research*, *105*(A2), 2413–2424. https://doi.org/10.1029/1999JA900439

Cnossen, I., Wiltberger, M., & Ouellette, J. E. (2012). The effects of seasonal and diurnal variations in the Earth's magnetic dipole orientation on solar wind-magnetosphere-ionosphere coupling. *Journal of Geophysical Research*, *117*(A11), A11211. https://doi.org/10.1029/2012JA017825

Cowley, S. W. H., & Lockwood, M. (1992). Excitation and decay of solar wind-driven flows in the magnetosphere-ionosphere system. *Annales Geophysicae*, *10*, 103–115.

Cowley, S. W. H., Morelli, J. P., & Lockwood, M. (1991). Dependence of convective flows and particle precipitation in the high-latitude dayside ionosphere on the X and Y components of the interplanetary magnetic field. *Journal of Geophysical Research*, *96*(A4), 5557. https://doi.org/10.1029/90JA02063

Coxon, J. C., Milan, S. E., & Anderson, B. J. (2018). A review of Birkeland current research using AMPERE. In A. Keiling, O. Marghitu, & M. Wheatland (Eds.), *Geophysical monograph series* (pp. 257–278). John Wiley & Sons, Inc. https://doi.org/10.1002/9781119324522.ch16

Crooker, N. U., & Siscoe, G. L. (1986). On the limits of energy transfer through dayside merging. *Journal of Geophysical Research*, *91*(A12), 13393–13397. https://doi.org/10.1029/JA091iA12p13393

Danilov, A. A., Krymskii, G. F., & Makarov, G. A. (2013). Geomagnetic activity as a reflection of processes in the magnetospheric tail: 1. The source of diurnal and semiannual variations in geomagnetic activity. *Geomagnetism and Aeronomy*, *53*(4), 441–447. https://doi.org/10.1134/S0016793213040051

de La Sayette, P., & Berthelier, A. (1996). The *am* annual-diurnal variations 1959-1988: A 30-year evaluation. *Journal of Geophysical Research*, *101*(A5), 10653–10663. https://doi.org/10.1029/96JA00165

Eggington, J. W. B., Eastwood, J. P., Mejnertsen, L., Desai, R. T., & Chittenden, J. P. (2020). Dipole tilt effect on magnetopause reconnection and the steady-state magnetosphere-ionosphere system: Global MHD simulations. *Journal of Geophysical Research: Space Physics*, *125*(7), e2019JA027510. https://doi.org/10.1029/2019JA027510

Finch, I. D., Lockwood, M. L., & Rouillard, A. P. (2008). Effects of solar wind magnetosphere coupling recorded at different geomagnetic latitudes: Separation of directly-driven and storage/release systems. *Geophysical Research Letters*, *35*(21), L21105. https://doi.org/10.1029/2008GL035399

Förster, M., & Cnossen, I. (2013). Upper atmosphere differences between northern and southern high latitudes: The role of magnetic field asymmetry. *Journal of Geophysical Research: Space Physics*, *118*(9), 5951–5966. https://doi.org/10.1002/jgra.50554

Forsyth, C., Rae, I. J., Coxon, J. C., Freeman, M. P., Jackman, C. M., Gjerloev, J., & Fazakerley, A. N. (2015). A new technique for determining substorm onsets and phases from indices of the electrojet (SOPHIE). *Journal of Geophysical Research: Space Physics*, *120*(12), 10592–10606. https://doi.org/10.1002/2015JA021343

Hairston, M. R., & Heelis, R. A. (1993). *High-latitude electric field studies using DMSP data*, Richardson Center for Space Sciences Report. University of Texas at Dallas. Retrieved from https://apps.dtic.mil/sti/pdfs/ADA265032.pdf

Hoilijoki, S., Souza, V. M., Walsh, B. M., Janhunen, P., & Palmroth, M. (2014). Magnetopause reconnection and energy conversion as influenced by the dipole tilt and the IMF B_x. *Journal of Geophysical Research: Space Physics*, *119*(6), 4484–4494. https://doi.org/10.1002/2013JA019693

Kabin, K., Rankin, R., Rostoker, G., Marchand, R., Rae, I. J., Ridley, A. J., et al. (2004). Open-closed field line boundary position: A parametric study using an MHD model. *Journal of Geophysical Research*, *109*(A5), A05222. https://doi.org/10.1029/2003JA010168

Kitamura, N., Hasegawa, H., Saito, Y., Shinohara, I., Yokota, S., Nagai, T., et al. (2016). Shift of the magnetopause reconnection line to the winter hemisphere under southward IMF conditions: Geotail and MMS observations. *Geophysical Research Letters*, *43*(11), 5581–5588. https://doi.org/10.1002/2016GL069095

Kivelson, M. G., & Hughes, W. J. (1990). On the threshold for triggering substorms. *Planetary and Space Science*, *38*(2), 211–220. https://doi.org/10.1016/0032-0633(90)90085-5

Koochak, Z., & Fraser-Smith, A. C. (2017). An update on the centered and eccentric geomagnetic dipoles and their poles for the years 1980–2015. *Earth and Space Science*, *4*(10), 626–636. https://doi.org/10.1002/2017EA000280

Korovinskiy, D. B., Semenov, V. S., Erkaev, N. V., Ivanov, I. B., & Kiehas, S. A. (2018). Current sheet bending as destabilizing factor in magnetotail dynamics. *Physics of Plasmas*, *25*(9), 092901. https://doi.org/10.1063/1.5046175

Kubota, Y., Nagatsuma, T., Den, M., Tanaka, T., & Fujita, S. (2017). Polar cap potential saturation during the Bastille Day storm event using global MHD simulation. *Journal of Geophysical Research: Space Physics*, *122*(4), 4398–4409. https://doi.org/10.1002/2016JA023851

Kubyshkina, M., Semenov, V., Erkaev, N., Gordeev, E., & Kubyshkin, I. (2022). The asymmetry of magnetospheric configuration and substorms occurrence rate within a solar activity cycle. Springer Proceedings in Earth and Environmental Sciences. In A. Kosterov, N. Bobrov, E. Gordeev, E. Kulakov, E. Lyskova, & I. Mironova (Eds.), *Problems of geocosmos–2020* (pp. 451–464). Springer International Publishing. https://doi.org/10.1007/978-3-030-91467-7_33

Kubyshkina, M., Tsyganenko, N., Semenov, V., Kubyshkina, D., Partamies, N., & Gordeev, E. (2015). Further evidence for the role of magnetotail current shape in substorm initiation. *Earth Planets and Space*, *67*(1), 139. https://doi.org/10.1186/s40623-015-0304-1

Laitinen, T., Janhunen, P., Pulkkinen, T., Palmroth, M., & Koskinen, H. (2006). On the characterization of magnetic reconnection in global MHD simulations. *Annales Geophysicae*, *24*(11), 3059–3069. https://doi.org/10.5194/angeo-24-3059-2006

Laundal, K. M., Cnossen, I., Milan, S. E., Haaland, S. E., Coxon, J., Pedatella, N. M., et al. (2017). North–south asymmetries in Earth's magnetic field: Effects on high-latitude geospace. *Space Science Reviews*, *206*(1–4), 225–257. https://doi.org/10.1007/s11214-016-0273-0

Li, H., Wang, C., & Peng, Z. (2013). Solar wind impacts on growth phase duration and substorm intensity: A statistical approach. *Journal of Geophysical Research: Space Physics*, *118*(7), 4270–4278. https://doi.org/10.1002/jgra.50399

Liou, K., Sotirelis, T., & Mitchell, E. (2020). Control of the east-west component of the Interplanetary Magnetic Field on the occurrence of magnetic substorms. *Geophysical Research Letters*, *47*(5), e2020GL087406. https://doi.org/10.1029/2020GL087406

Livermore, P., Finlay, C. C., & Bayliff, M. (2020). Recent north magnetic pole acceleration towards Siberia caused by flux lobe elongation. *Nature Geoscience*, *13*(5), 387–391. https://doi.org/10.1038/s41561-020-0570-9

Lockwood, M. (1991). On flow reversal boundaries and transpolar voltage in average models of high-latitude convection. *Planetary and Space Science*, *39*(3), 397–409. https://doi.org/10.1016/0032-0633(91)90002-R

Lockwood, M. (1993). Modelling high-latitude ionosphere for time-varying plasma convection. *IEE Proceedings H Microwaves, Antennas and Propagation*, *140*(2), 91. https://doi.org/10.1049/ip-h-2.1993.0015

Lockwood, M. (2013). Reconstruction and prediction of variations in the open solar magnetic flux and interplanetary conditions. *Living Reviews in Solar Physics*, *10*, 1–88. https://doi.org/10.12942/lrsp-2013-4

Lockwood, M. (2022). Solar wind—Magnetosphere coupling functions: Pitfalls, limitations, and applications. *Space Weather*, *20*(2), e2021SW002989. https://doi.org/10.1029/2021SW002989

Lockwood, M. (2023). Northern and Southern hemisphere Polar Cap Indices: To what extent do they agree and to what extent should they agree? *Journal of Geophysical Research: Space Physics*, *128*(7), e2023JA031464. https://doi.org/10.1029/2023JA031464

Lockwood, M., Chambodut, A., Finch, I. D., Barnard, L. A., Owens, M. J., & Haines, C. (2019). Time-of-day/time-of-year response functions of planetary geomagnetic indices. *Journal of Space Weather and Space Climate*, *9*, A20. https://doi.org/10.1051/swsc/2019017

Lockwood, M., Cowley, S., Todd, H., Willis, D., & Clauer, C. (1988). Ion flows and heating at a contracting polar-cap boundary. *Planetary and Space Science*, *36*(11), 1229–1253. https://doi.org/10.1016/0032-0633(88)90076-1

Lockwood, M., & Cowley, S. W. H. (2022). Magnetosphere-ionosphere coupling: Implications of non-equilibrium conditions. *Frontiers in Astronomy and Space Sciences*, *9*, 908571. https://doi.org/10.3389/fspas.2022.908571

Lockwood, M., Haines, C., Barnard, L. A., Owens, M. J., Scott, C. J., Chambodut, A., & McWilliams, K. A. (2021). Semi-annual, annual and universal time variations in the magnetosphere and in geomagnetic activity: 4. Polar cap motions and origins of the universal time effect. *Journal of Space Weather and Space Climate*, *11*, 15. https://doi.org/10.1051/swsc/2020077

Lockwood, M., Hairston, M., Finch, I. D., & Rouillard, A. P. (2009). Transpolar voltage and polar cap flux during the substorm cycle and steady convection events. *Journal of Geophysical Research*, *114*(A1), A01210. https://doi.org/10.1029/2008JA013697

Lockwood, M., & McWilliams, K. A. (2021a). On optimum solar wind-magnetosphere coupling functions for transpolar voltage and planetary geomagnetic activity. *Journal of Geophysical Research: Space Physics*, *126*(12), e2021JA029946. https://doi.org/10.1029/2021JA029946

Lockwood, M., & McWilliams, K. A. (2021b). A survey of 25 years' transpolar voltage data from the SuperDARN radar network and the expanding-contracting polar cap model. *Journal of Geophysical Research: Space Physics*, *126*(9), e2021JA029554. https://doi.org/10.1029/2021JA029554

Lockwood, M., McWilliams, K. A., Owens, M. J., Barnard, L. A., Watt, C. E., Scott, C. J., et al. (2020). Semi-annual, annual and universal time variations in the magnetosphere and in geomagnetic activity: 2. Response to solar wind power input and relationships with solar wind dynamic pressure and magnetospheric flux transport. *Journal of Space Weather and Space Climate*, *10*, 30. https://doi.org/10.1051/swsc/2020033

Lockwood, M., & Milan, S. E. (2023). Universal time variations in the magnetosphere. *Frontiers in Astronomy and Space Sciences*, *10*(9), 1139295. https://doi.org/10.3389/fspas.2023.1139295

Lockwood, M., Owens, M., & Barnard, L. (2023). Universal Time variations in the magnetosphere and the effect of CME arrival time: Analysis of the February 2022 event that led to the loss of Starlink satellites. *Journal of Geophysical Research: Space Science*. https://doi.org/10.1002/essoar.10512909.1

Lockwood, M., Owens, M. J., Barnard, L. A., Haines, C., Scott, C. J., McWilliams, K. A., & Coxon, J. C. (2020). Semi-annual, annual and universal time variations in the magnetosphere and in geomagnetic activity: 1. Geomagnetic data. *Journal of Space Weather and Space Climate*, *10*, 23. https://doi.org/10.1051/swsc/2020023

Lockwood, M., Owens, M. J., Barnard, L. A., Watt, C. E., Scott, C. J., Coxon, J. C., & McWilliams, K. A. (2020). Semi-annual, annual and universal time variations in the magnetosphere and in geomagnetic activity: 3. Modelling. *Journal of Space Weather and Space Climate*, *10*, 61. https://doi.org/10.1051/swsc/2020062

Lyatsky, W., Newell, P. T., & Hamza, A. (2001). Solar illumination as cause of the equinoctial preference for geomagnetic activity. *Geophysical Research Letters*, *28*(12), 2353–2356. https://doi.org/10.1029/2000GL012803

Lyons, L. R., Zou, Y., Nishimura, Y., Gallardo-Lacourt, B., Angelopulos, V., & Donovan, E. F. (2018). Stormtime substorm onsets: Occurrence and flow channel triggering. *Earth Planets and Space*, *70*(1), 81. https://doi.org/10.1186/s40623-018-0857-x

Mayaud, P.-N. (1972). The aa indices: A 100-year series characterizing the magnetic activity. *Journal of Geophysical Research*, *77*(34), 6870–6874. https://doi.org/10.1029/ja077i034p06870

McIntosh, D. (1959). On the annual variation of magnetic disturbance. *Philosophical Transactions of the Royal Society of London - Series A: Mathematical and Physical Sciences*, *251*(1001), 525–552. https://doi.org/10.1098/rsta.1959.0010

McWilliams, K., Pfeifer, J., & McPherron, R. (2008). Steady magnetospheric convection selection criteria: Implications of global SuperDARN convection measurements. *Geophysical Research Letters*, *35*(9), L09102. https://doi.org/10.1029/2008GL033671

Menvielle, M., & Berthelier, A. (1991). The *K*-derived planetary indices: Description and availability. *Reviews of Geophysics*, *29*(3), 415–432. https://doi.org/10.1029/91RG00994

Milan, S. E., Boakes, P. D., & Hubert, B. (2008). Response of the expanding/contracting polar cap to weak and strong solar wind driving: Implications for substorm onset. *Journal of Geophysical Research*, *113*(A9), A09215. https://doi.org/10.1029/2008JA013340

Milan, S. E., Carter, J. A., Sangha, H., Bower, G. E., & Anderson, B. J. (2021). Magnetospheric flux throughput in the Dungey cycle: Identification of convection state during 2010. *Journal of Geophysical Research: Space Physics*, *126*(2), e2020JA028437. https://doi.org/10.1029/2020JA028437

Milan, S. E., Grocott, A., & Hubert, B. (2010). A superposed epoch analysis of auroral evolution during substorms: Local time of onset region. *Journal of Geophysical Research*, *115*(A5), A00I04. https://doi.org/10.1029/2010JA015663

Milan, S. E., Mooney, M., Bower, G., Fleetham, A., Vines, S., & Gjerloev, J. (2023). Solar wind-magnetosphere coupling during Hildcaas. *Journal Geophysical Research: Space Physics*. https://doi.org/10.22541/essoar.169447432.22694279

Milan, S. E., Walach, M., Carter, J. A., Sangha, H., & Anderson, B. J. (2019). Substorm onset latitude and the steadiness of magnetospheric convection. *Journal of Geophysical Research: Space Physics*, *124*(3), 1738–1752. https://doi.org/10.1029/2018JA025969

Mishin, V., Karavaev, Y., & Караваев, Ю. (2017). Saturation of the magnetosphere during superstorms: New results from the magnetogram inversion technique. *Solar-Terrestrial Physics*, *3*(3), 28–36. https://doi.org/10.12737/stp-33201704

Moen, J., & Brekke, A. (1993). The solar flux influence on quiet time conductances in the auroral ionosphere. *Geophysical Research Letters*, *20*(10), 971–974. https://doi.org/10.1029/92GL02109

Nagatsuma, T. (2004). Conductivity dependence of cross-polar potential saturation. *Journal of Geophysical Research*, *109*(A4), A04210. https://doi.org/10.1029/2003JA010286

Newell, P. T., & Gjerloev, J. W. (2011a). Evaluation of SuperMAG auroral electrojet indices as indicators of substorms and auroral power. *Journal of Geophysical Research*, *116*(A12), 2011JA016779. https://doi.org/10.1029/2011JA016779

Newell, P. T., & Gjerloev, J. W. (2011b). Substorm and magnetosphere characteristic scales inferred from the SuperMAG auroral electrojet indices. *Journal of Geophysical Research*, *116*(A12), 2011JA016936. https://doi.org/10.1029/2011JA016936

Newell, P. T., & Gjerloev, J. W. (2012). SuperMAG-based partial ring current indices. *Journal of Geophysical Research*, *117*(A5), 2012JA017586. https://doi.org/10.1029/2012JA017586

Newell, P. T., Sotirelis, T., Skura, J. P., Meng, C.-I., & Lyatsky, W. (2002). Ultraviolet insolation drives seasonal and diurnal space weather variations. *Journal of Geophysical Research*, *107*(A10), 1305. https://doi.org/10.1029/2001JA000296

Østgaard, S., Mende, S. B., Frey, H., Immel, T., Frank, L., Sigwarth, J., & Stubbs, T. (2004). Interplanetary magnetic field control of the location of substorm onset and auroral features in the conjugate hemispheres. *Journal of Geophysical Research*, *109*(A7), A07204. https://doi.org/10.1029/2003JA010370

Ou, J., Du, A., Ge, Y., Luo, H., Zhang, Y., & Guo, Z. (2022). Statistical study on the North-South asymmetric distribution of the mid-low-latitude nightside disturbed magnetic fields. *Journal of Geophysical Research: Space Physics*, *127*(3), e2021JA029970. https://doi.org/10.1029/2021JA029970

Park, K. S., Ogino, T., & Walker, R. J. (2006). On the importance of antiparallel reconnection when the dipole tilt and IMF B_y are nonzero. *Journal of Geophysical Research*, *111*(A5), A05202. https://doi.org/10.1029/2004JA010972

Pitkänen, T., Hamrin, M., Kullen, A., Maggiolo, R., Karlsson, T., Nilsson, H., & Norqvist, P. (2016). Response of magnetotail twisting to variations in IMF B_y: A THEMIS case study 1–2 January 2009. *Geophysical Research Letters*, *43*(15), 7822–7830. https://doi.org/10.1002/2016GL070068

Ridley, A. J., Gombosi, T. I., & DeZeeuw, D. L. (2004). Ionospheric control of the magnetosphere: Conductance. *Annales Geophysicae*, *22*(2), 567–584. https://doi.org/10.5194/angeo-22-567-2004

Russell, C. T., & McPherron, R. L. (1973). Semiannual variation of geomagnetic activity. *Journal of Geophysical Research*, *78*(1), 92–108. https://doi.org/10.1029/JA078i001p00092

Russell, C. T., Wang, Y. L., & Raeder, J. (2003). Possible dipole tilt dependence of dayside magnetopause reconnection. *Geophysical Research Letters*, *30*(18), 1937. https://doi.org/10.1029/2003GL017725

Spence, H. E. (1996). The what, where, when, and why of magnetospheric substorm triggers. *Eos, Transactions American Geophysical Union*, *77*(9), 81–86. https://doi.org/10.1029/96EO00051

Stauning, P. (2007). A new index for the interplanetary merging electric field and geomagnetic activity: Application of the unified polar cap indices. *Space Weather*, *5*(9), S09001. https://doi.org/10.1029/2007SW000311

Tanaka, T., Ebihara, Y., Watanabe, M., Den, M., Fujita, S., Kikuchi, T., et al. (2021). Roles of the M-I coupling and plasma sheet dissipation on the growth-phase thinning and subsequent transition to the onset. *Journal of Geophysical Research: Space Physics*, *126*(12), e2021JA029925. https://doi.org/10.1029/2021JA029925

Tanskanen, E. I., Pulkkinen, T. I., Viljanen, A., Mursula, K., Partamies, N., & Slavin, J. A. (2011). From space weather toward space climate time scales: Substorm analysis from 1993 to 2008. *Journal of Geophysical Research*, *116*(A5), A00I34. https://doi.org/10.1029/2010JA015788

Thébault, E., Finlay, C. C., Beggan, C. D., Alken, P., Aubert, J., Barrois, O., et al. (2015). International geomagnetic reference field: The 12th generation. *Earth Planets and Space*, *67*(1), 79. https://doi.org/10.1186/s40623-015-0228-9

Tóth, G., Sokolov, I., Gombosi, T., Chesney, D., Clauer, C., De Zeeuw, D., et al. (2005). Space weather modeling Framework: A new tool for the space science community. *Journal of Geophysical Research*, *110*(A12), A12226. https://doi.org/10.1029/2005JA011126

Trattner, K. J., Petrinec, S. M., Fuselier, S. A., & Phan, T. D. (2012). The location of reconnection at the magnetopause: Testing the maximum magnetic shear model with THEMIS observations. *Journal of Geophysical Research*, *117*(A1), 2011JA016959. https://doi.org/10.1029/2011JA016959

Troshichev, O. (2022). PC index as a ground-based indicator of the solar wind energy incoming into the magnetosphere: (1) relation of PC index to the solar wind electric field EKL. *Frontiers in Astronomy and Space Sciences*, *9*, 1069470. https://doi.org/10.3389/fspas.2022.1069470

Tsurutani, B., Echer, E., Guarnieri, F., & Gonzalez, W. (2011). The properties of two solar wind high speed streams and related geomagnetic activity during the declining phase of solar cycle 23. *Journal of Atmospheric and Solar-Terrestrial Physics*, *73*(1), 164–177. https://doi.org/10.1016/j.jastp.2010.04.003

Tulegenov, B., Raeder, J., Cramer, W. D., Ferdousi, B., Fuller-Rowell, T. J., Maruyama, N., & Strangeway, R. J. (2023). Storm time polar cap expansion: Interplanetary magnetic field clock angle dependence. *Annales Geophysicae*, *41*(1), 39–54. https://doi.org/10.5194/angeo-41-39-2023

Wang, H., & Lühr, H. (2007). Seasonal-longitudinal variation of substorm occurrence frequency: Evidence for ionospheric control. *Geophysical Research Letters*, *34*(7), L07104. https://doi.org/10.1029/2007GL029423

Wang, H., Zhang, K. D., Wan, X., & Lühr, H. (2017). Universal time variation of high-latitude thermospheric disturbance wind in response to a substorm. *Journal of Geophysical Research: Space Physics*, *122*(4), 4638–4653. https://doi.org/10.1002/2016JA023630

Zhang, B., Lotko, W., Brambles, O., Wiltberger, M., & Lyon, J. (2015). Electron precipitation models in global magnetosphere simulations. *Journal of Geophysical Research: Space Physics*, *120*(2), 1035–1056. https://doi.org/10.1002/2014JA020615

Zhao, H., & Zong, Q.-G. (2012). Seasonal and diurnal variation of geomagnetic activity: Russell-McPherron effect during different IMF polarity and/or extreme solar wind conditions. *Journal of Geophysical Research*, *117*(A11), A11222. https://doi.org/10.1029/2012JA017845

Zhu, C. B., Zhang, H., Ge, Y. S., Pu, Z. Y., Liu, W. L., Wan, W. X., et al. (2015). Dipole tilt angle effect on magnetic reconnection locations on the magnetopause. *Journal of Geophysical Research: Space Physics*, *120*(7), 5344–5354. https://doi.org/10.1002/2015JA020989

Zou, Y., Lyons, L., Conde, M., Varney, R., Angelopoulos, V., & Mende, S. (2021). Effects of substorms on high-latitude upper thermospheric winds. *Journal of Geophysical Research: Space Physics*, *126*(1), e2020JA028193. https://doi.org/10.1029/2020JA028193